Accepted by ApJ Main Journal on 2014 July 16
Preprint typeset using LaTeX style emulateapj v. 5/2/11

arXiv:1407.4857v1 [astro-ph.GA] 17 Jul 2014

A DYNAMICALLY COLLAPSING CORE AND A PRECURSOR OF A CORE IN A FILAMENT SUPPORTED BY TURBULENT AND MAGNETIC PRESSURES

Ray S. Furuya[1]
Center for General Education, the University of Tokushima

Yoshimi Kitamura[2]
Institute of Space and Astronautical Science, Japan Aerospace Exploration Agency

and

Hiroko Shinnaga[3]
Chile Observatory, National Astronomical Observatory of Japan

Accepted by ApJ Main Journal on 2014 July 16

ABSTRACT

To study physical properties of the natal filament gas around the cloud core harboring an exceptionally young low-mass protostar GF 9-2, we carried out $J = 1 - 0$ line observations of ^{12}CO, ^{13}CO, and C^{18}O molecules using the Nobeyama 45 m telescope. The mapping area covers $\sim 1/5$ of the whole filament. Our ^{13}CO and C^{18}O maps clearly demonstrate that the core formed at the local density maxima of the filament, and the internal motions of the filament gas are totally governed by turbulence with Mach number of $\sim$2. We estimated the scale height of the filament to be $H = 0.3 \sim 0.7$ pc, yielding the central density of $n_{\rm c} = 700 \sim 4200$ cm^{-3}. Our analysis adopting an isothermal cylinder model shows that the filament is supported by the turbulent and magnetic pressures against the radial and axial collapse due to self-gravity. Since both the dissipation time scales of the turbulence and the transverse magnetic fields can be comparable to the free-fall time of the filament gas of 10^6 years, we conclude that the local decay of the supersonic turbulence made the filament gas locally unstable, hence making the core collapse. Furthermore, we newly detected a gas condensation with velocity width enhancement to $\sim$0.3 pc south-west of the GF 9-2 core. The condensation has a radius of $\sim$0.15 pc and an LTE mass of $\sim 5\ M_\odot$. Its internal motion is turbulent with Mach number of $\sim$3, suggestive of a gravitationally unbound state. Considering the uncertainties in our estimates, however, we propose that the condensation is a precursor of a cloud core which would have been produced by the collision of the two gas components identified in the filament.

Subject headings: ISM: clouds — ISM: evolution — ISM: individual (GF 9–2, L 1082C, PSC 20503+6006) — turbulence — stars: formation — stars: pre-main sequence

1. INTRODUCTION

Filamentary molecular clouds, filaments, are now considered to be one of the evolutionary stages for the interstellar medium to evolve from molecular clouds to stars. Analyzing dark globular filaments identified in optical images, Schneider & Elmegreen (1979) pointed out that a filament would fragment into equally spaced condensations of gas and dust due to its gravity. Indeed molecular line observations in the 1980s showed that filaments contain such condensations, dense molecular cloud cores, which are now known to be the immediate sites of star formation. This hierarchical structure is typically seen in nearby low-mass star forming regions such as the Taurus molecular cloud (e.g., Palla & Stahler 2002, and references therein). Recently our knowledge about filaments is significantly improved by systematic far-infrared (FIR) imaging survey of the thermal emission from the interstellar dust using *Herschel* Space Observatory (André et al. 2010, and references therein). FIR images taken with *Herschel* demonstrated that molecular clouds have ubiquitous networks of filaments which are highly likely produced through the interaction among gravity, interstellar turbulence and magnetic field. These observations clearly suggest that in general dense cores originate in the fragmentation process of filaments. Another important results from the *Herschel* observations is that filaments are omnipresent even in non-star forming cloud complexes (e.g., Men'shchikov et al. 2010).

On the other hand, theoretical studies have long discussed that molecular clouds collapse into sheet-like clouds which are formed through a compression process such as cloud-cloud collision, and that the sheet-like clouds fragment to filamentary clouds which will form dense cloud cores (e.g., Miyama et al. 1984). Considering balance between self-gravity and pressure gradient in radial direction of a cylinder, Stodólkiewicz (1963) and Ostriker (1964) found that a filament radially collapses if the line mass (the mass per unit length) of the filament exceeds the critical value of $2c_{\rm s}^2/G$ where $c_{\rm s}$ is the isothermal sound speed and G is the gravitational constant. Stability of a cylinder in equilibrium against axial perturbations was studied for the isother-

rsf@tokushima-u.ac.jp
kitamura@isas.jaxa.jp
hiroko.shinnaga@nao.ac.jp
[1] Minami Jousanjima-Machi 1-1, Tokushima, Tokushima 770-8502, Japan
[2] Yoshinodai 3-1-1, Sagamihara, Kanagawa 229-8510, Japan
[3] Osawa 2-21-1, Mitaka, Tokyo 181-8588, Japan

mal incompressible cylinder composed of polytropic gas by Chandrasekhar & Fermi (1953b): they found critical wave numbers against the axial fragmentation, but such an unstable cylinder can be stabilized by the axial magnetic fields of (0, 0, B_z) in the cylindrical coordinate. Stodólkiewicz (1963) studied how stability of the compressible gas depends on the magnetic fields: the critical wavelength becomes longer for (0, B_ϕ, 0), whereas does short for (0, 0, B_z). In contrast, Nagasawa (1987) showed that critical wavelengths do not change with a uniform (0, 0, B_z), but the growth rates of the unstable modes are suppressed, which differs from the conclusion drawn from the Stodolkiewicz's calculations. As summarized in Larson (1985), all the studies showed that a filament breaks into "clumps" with a separation of about 4 times the diameter of the cylinder. Inutsuka & Miyama (1997) investigated the axial fragmentation and radial collapse of a cylinder in more detail; they showed that merging and clustering of newly formed "clumps" occur within a time scale of the fragmentation process of the natal filaments.

Although details remain a matter of debate, several unstable modes for the filament fragmentation are proposed by modern numerical simulations (see reviews by e.g., Mac Low & Klessen 2004; André et al. 2009, and references therein). These simulations may be categorized by the roles of magnetic fields and turbulence being considered. In principal, a complex interplay between magnetic fields plus turbulence and self-gravity of the cloud are believed to control the duration of core formation. One scenario is the "fast mode" with weak magnetic field (e.g., Padoan & Nordlund 1999; Padoan et al. 2001; Hartmann et al. 2001; Klessen et al. 2000, 2005; Krumholz & McKee 2005; Krumholz & Tan 2007). The opposite is the "slow mode" with strong magnetic field (e.g., Allen & Shu 2000; Elmegreen 2007; Nakamura & Li 2005, 2008). The difference between the "fast" and "slow" modes is whether or not a core forms within free-fall time of the natal gas. All the 3D simulations predict formation of network of filaments, but their complexity in velocity fields differs significantly (see review by André et al. 2009). In general, the "slow mode" expects quiescent ambient velocity field controlled by magnetic field, whereas the "fast mode" predicts large scale supersonic velocity field. In other words, physical properties of the low density gas in the filament are considered to determine the formation mechanism and evolution of the dense cores.

To link physical properties of such low density gas to our knowledge about collapse of a cloud core, we performed a detailed study of the dense cloud core GF 9-2 which is also known as L1082C (e.g., Bontemps et al. 1996; Caselli et al. 2002, and references therein). This core contains an extremely young low-mass protostar (Furuya et al. 2006, hereafter paper I) whose circumstellar materials are probably responsible for the IRAS point source PSC 20503+6006 (e.g., Ciardi et al. 1998). The core has been identified by several molecular lines such as CS (2–1) (Ciardi et al. 2000), N_2H^+ (1–0) (Caselli et al. 2002; paper I), $H^{13}CO^+$ (1–0), NH_3(1,1), and CCS 4_3-3_2 lines (paper I). The core is located in the GF 9 filament (d = 200 pc) which is the ninth filament cataloged in Schneider & Elmegreen (1979). Using the optical image Schneider & Elmegreen (1979) estimated a total length of the filament to be 1.25°, corresponding to 4.4 pc, although the filament curves as a portion of a shell. The filament contains almost equally spaced seven dense cores identified in the NH_3(1,1) lines (Furuya et al. 2008, hereafter paper II). The physical properties of the filament were subsequently studied by near-infrared (NIR) extinction (Ciardi et al. 2000), and optical and NIR polarization observations (Poidevin & Bastien 2006). In particular, Poidevin & Bastien (2006) revealed that there exists a well aligned large scale magnetic field, and claimed that the field is almost perpendicular to the axis of the filament as the first order approximation.

The protostar harbored in the GF 9-2 core has not developed an extensive molecular outflow (Bontemps et al. 1996; paper I). This fact yields a rare opportunity to investigate core collapse conditions free from the disturbance by the outflow. Our previous studies towards the core using the Nobeyama 45 m telescope, CSO 10.4 m telescope and the OVRO mm-array showed that the GF 9-2 core has a radial density profile of $\rho(r) \propto r^{-2}$ (paper I). Furthermore we detected blueskewed profiles in optically thick lines of HCO^+ (3–2), (1–0), and HCN (1–0), suggestive of gas infall motions all over the core (Furuya et al. 2009, hereafter paper III). Modeling the infall spectra, we pointed out that the core has undergone its gravitational collapse for $\sim 2\times10^5$ years from an initially unstable state in paper III. This is because the observed radial density profile was between those predicted in the runaway collapse scenario (Larson 1969; Penston 1969; Hunter 1977; the LPH solution) and the quasi-static inside-out collapse scenario (Shu 1977), and because the observed velocity field inside the core has a reasonable consistency with that expected from the former scenario. However, it was impossible to investigate what had triggered the dynamical collapse of the core based on the data tracing only high density molecular gas [$10^5 \lesssim n(H_2)/cm^{-3} \lesssim 10^6$]. Clearly it required to unveil a close link between the initial conditions of the collapse and the physical properties of the low density ambient gas in the filament. We therefore carried out wide-field spectroscopic observations of the low density [$10^3 \lesssim n(H_2)/cm^{-3} \lesssim 10^4$] gas in the filament using the Nobeyama 45 m telescope.

Contrary to the previous papers which dealt with the dense core gas, this paper presents a detailed observational study of the low density natal filament gas surrounding the dense core GF 9-2. The organization of this paper is as follows: §2 describes the observations; §3 summarizes the results which were directly derived from the obtained spectra and maps of the CO emission; §4 describes our analysis of the excitation conditions of the CO lines, the velocity structure of the filament gas and the calculations of column density; §5 discusses the physical properties of the natal filament gas and a scenario of dense core formation; and §6 gives a summary of this work. Finally, details of our analysis presented in §4 as well as the associated error calculations are described in Appendix.

2. OBSERVATIONS

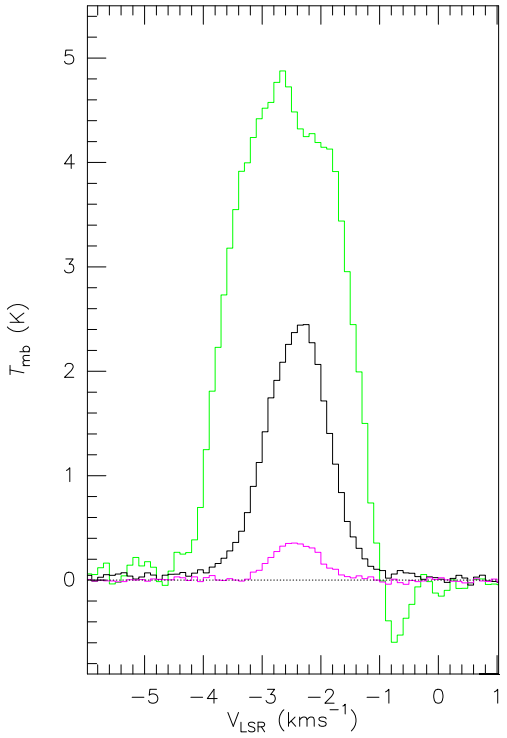

Figure 1. Spectra of the $J = 1 - 0$ lines of ^{12}CO (green), ^{13}CO (black), and C^{18}O (magenta) averaged over the whole region observed in the GF 9 filament with a beam size (HPBW) of 24″. The vertical scale of the plot is the main-beam brightness temperature ($T_{\rm mb}$) in K unit. The velocity resolutions of the spectra are 0.1 km s^{-1}. The RMS noise levels are 760 mK for ^{12}CO, 360 mK for ^{13}CO, and 130 mK for C^{18}O. The systemic velocity of the GF 9-2 dense cloud core is $V_{\rm LSR} = -2.48$ km s^{-1} (paper I). The negative dip seen in the ^{12}CO spectrum around $V_{\rm LSR} \sim -0.8$ km s^{-1} is an artifact caused by the presence of emission at the off-position (see §2).

Using the Nobeyama Radio Observatory (NRO)[4] 45 m telescope, we carried out On-The-Fly (OTF) mapping observations (Sawada et al. 2008) of the J =1–0 transitions of ^{12}C^{16}O [rest frequency ($\nu_{\rm rest}$) =115271.202 MHz], ^{13}C^{16}O ($\nu_{\rm rest}$ =110201.353 MHz), and ^{12}C^{18}O ($\nu_{\rm rest}$ =109782.173 MHz) towards a portion of the GF 9 filament. Our OTF mapping was performed over a square region of 800″ × 800″ centered on the position of the 3 mm continuum source (R.A. = 20$^{\rm h}$51$^{\rm m}$29.″827, Decl. =60°18′38.″06 in J2000; paper I). Notice that the two adjacent dense cores of GF 9-3 (angular separation of 910″, corresponding to 0.88 pc to the east; paper II) and GF 9-1 (740″ = 0.71 pc to the west) are not included in the observed area. The observations were done in an LST range of 17^h – 2^h over 7 days in 2008 March. We used the 25 Beam Array Receiver System (BEARS), and configured auto-correlators (ACs) as a backend, yielding a velocity resolution ($\Delta v_{\rm res}$) of 0.039 km s^{-1} for the ^{13}CO and C^{18}O lines in an 8 MHz bandwidth mode. For the ^{12}CO line, we employed a coarse velocity resolution mode of a 16 MHz bandwidth, providing $\Delta v_{\rm res}$ of 0.074 km s^{-1}. At 112 GHz, the mean beam size ($\theta_{\rm HPBW}$) of the 25 beams was estimated to be 14.″9 by the observatory. The mean main-beam efficiencies ($\eta_{\rm mb}$) for the 25 beams were 40±2% at 110 GHz, and 32±2% at 115 GHz. All the spectra were calibrated by the standard chopper wheel method, and were converted into main-beam brightness temperature ($T_{\rm mb}$) by dividing by $\eta_{\rm mb}$. The uncertainty in our intensity calibration is ∼15%. The telescope pointing was checked every 1.2 hrs by observing the SiO $J = 1 - 0$ $v = 1$ and $v = 2$ maser lines, and was found to be accurate to less than 3″. The data reduction was done using the NOSTAR package (Sawada et al. 2008). We produced 3-dimensional (3D) data cubes for the lines with an effective spatial resolution in FWHM of 24″, and an effective velocity resolution of 0.10 km s^{-1}. For producing the 3D cubes, we adopted a pixel size of 12″, and spatially smoothed the original data by convolving a Gaussian function with FWHM = 18.″9 to obtain the final effective resolution of 24″, while we applied no smoothing along the velocity axis.

[4] Nobeyama Radio Observatory is a branch of the National Astronomical Observatory of Japan, National Institutes of Natural Sciences.

3. RESULTS

Figure 1 shows $J = 1 - 0$ transition spectra of ^{12}CO, ^{13}CO, and C^{18}O molecules in $T_{\rm mb}$ obtained by averaging all the data. The ^{12}CO line is the brightest with the peak $T_{\rm mb}$ of ∼5 K, and seems to have a self-absorption feature over the LSR-velocity ($V_{\rm LSR}$) range of −2.6 to −1.8 km s^{-1}. The ^{13}CO and C^{18}O lines show single-peaked profiles. These peaks fall in the $V_{\rm LSR}$ range where the ^{12}CO line shows the self-absorption and the peak velocities agree with the systemic velocity ($V_{\rm sys}$) of the GF 9-2 dense core ($V_{\rm LSR} = -2.48$ km s^{-1}; paper I). Averaging the ^{12}CO and ^{13}CO spectra in a circle with a 50″ diameter towards the core, we verified consistency with those taken with the FCRAO 14 m telescope (Ciardi et al. 1998) in terms of the peak intensities and the spectral shapes.

We present total integrated intensity maps of the three CO isotopologues in Figure 2 where the total map of a dense gas tracer, H^{13}CO$^+$ (1–0) emission (paper I), is overlaid to assess spatial relations with the GF 9-2 dense cloud core. The ^{12}CO emission is detected all over the mapped area, and becomes intense to the south-west of the core. On the other hand, the ^{13}CO emission clearly represents a portion of the GF 9 filamentary dark cloud (Schneider & Elmegreen 1979), which is elongated along the east-west direction. The ^{13}CO emission becomes intense towards south-west, as seen in the ^{12}CO map. In the central region, the C^{18}O emission is elongated along northeast-southwest (Figure 2f), which agrees with the elongation of the core traced by e.g., the H^{13}CO$^+$ (1–0), N_2H^+ (1–0) (paper I), and ^{13}CO (1–0) (Ciardi et al. 1998) lines. These results clearly indicate that the C^{18}O line probes the gas with a medium density between those traced by the ^{13}CO and H^{13}CO$^+$ lines. Consequently, we have a seamless data set over a volume density range of $10^2 \lesssim n({\rm H_2})/{\rm cm^{-3}} \lesssim 10^6$.

Velocity channel maps with a resolution of 0.2 km s^{-1} are shown in Figures 3 and 4 where we overlaid the channel maps for the higher-density gas tracer with green contours on those for the lower-density gas tracer with black contours. First, the large-scale east-west structure is mainly seen in the ^{13}CO panels of $-3.9 \lesssim V_{\rm LSR}/{\rm km\ s^{-1}} \lesssim -2.3$. This velocity range includes the $V_{\rm sys}$ of the GF 9-

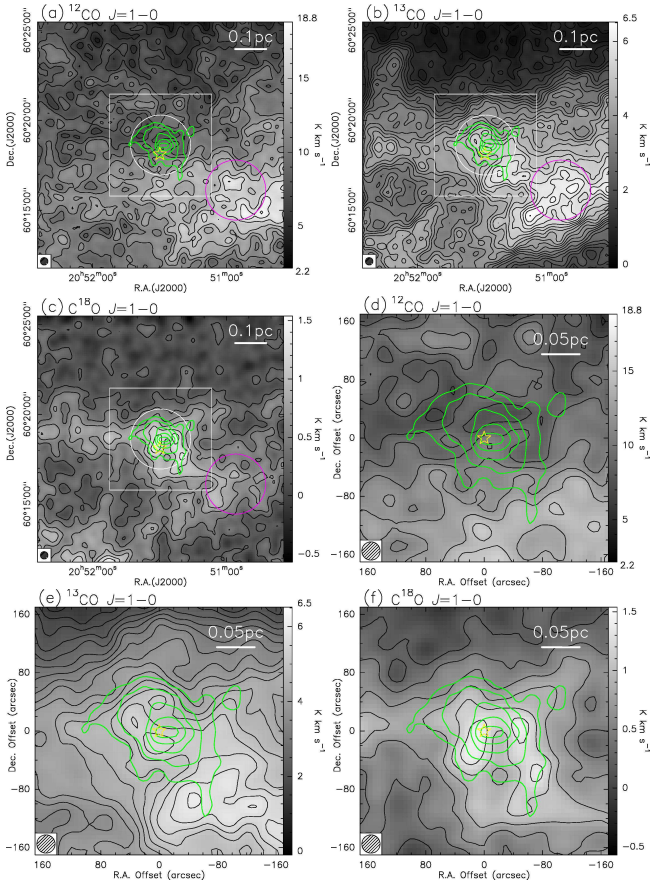

Figure 2. Total integrated intensity maps (greyscale plus thin contour) of the ^{12}CO (1–0) (left), ^{13}CO (1–0) (middle) and C^{18}O (1–0) (right) lines of the GF 9 filamentary cloud towards the dense cloud core GF 9-2. The green contours represent the total map of the H^{13}CO$^+$ (1–0) emission (paper I). The upper panels show all the observed area ($800''\times800''$) in the celestial coordinates, while the lower panels present the close-up views of the central $320''\times320''$ region in the offset coordinates with respect to the 3 mm continuum position (R.A. = $20^{\rm h}51^{\rm m}29\overset{s}{.}827$, Decl. $=60°18'38\overset{''}{.}06$ in J2000; paper I) designated by the yellow star. The white boxes in the upper panels indicate the area shown in the lower panels. The two circles in the upper panels are the areas where the emission were integrated to obtain the spectra shown in Figure 5. The hatched circle at the bottom left corner of each panel indicates the effective spatial resolution of $24''$, and the scale bars of 0.1 and 0.05 pc are indicated at the top right corners in the upper and lower panels, respectively. The ^{12}CO, ^{13}CO, and C^{18}O emissions are integrated over the LSR-velocity ranges of $-4.2 \le V_{\rm LSR}/{\rm km\ s^{-1}} \le -0.70$, $-3.9 \le V_{\rm LSR}/{\rm km\ s^{-1}} \le -0.80$, and $-3.2 \le V_{\rm LSR}/{\rm km\ s^{-1}} \le -1.6$, respectively, using the original data cubes with the velocity resolution of 0.10 km s^{-1}(§2). The ^{12}CO emission is detected all over the observed region, and its intensity ranges between 2.16 and 18.8 K km s^{-1}, corresponding to the 5.0σ and 43.4σ levels, respectively. We therefore plot the ^{12}CO contours starting from the 43σ level down to the 4σ level at 3σ intervals. The contours for the ^{13}CO and C^{18}O lines start from the 3σ levels with the 3σ intervals. Here the RMS noise (the 1σ) levels of the images are 0.43 K·km s^{-1} for ^{12}CO, 0.094 K·km s^{-1} for ^{13}CO, and 0.072 K·km s^{-1} for C^{18}O. The noise level in each map was estimated from a noise map created by integrating emission-free channels over the same velocity width as in the total emission map.

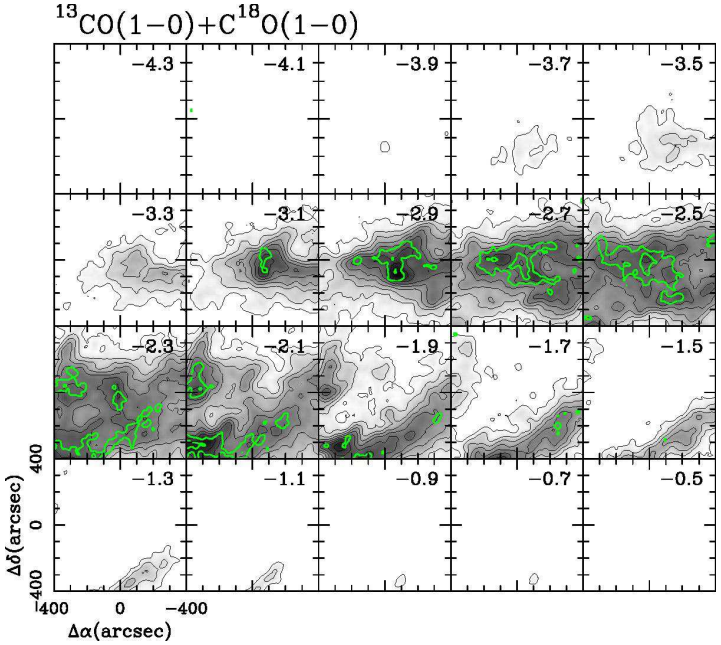

Figure 3. Velocity channel maps of the ^{13}CO (1–0) (greyscale plus black contours) and C^{18}O (1–0) (green contours) emission. All the contours are plotted at 5σ intervals starting from the 5σ levels where $\sigma = 300$ mK and 100 mK in $T_{\rm mb}$ for the ^{13}CO and C^{18}O lines, respectively. Each channel map is averaged over a 0.2 km s^{-1} bin whose central LSR-velocity is shown in unit of km s^{-1} at the top right corner of each panel.

2 dense core (-2.48 km s^{-1}). Hereafter, we refer to the east-west structure seen in the velocity range as "Component 1". Second, the Component 1 is likely to have sub-structures with scales of $\lesssim$0.1 pc ($100''$ corresponds to 0.097 pc at $d = 200$ pc), one of which is the GF 9-2 core. Third, one finds an overall agreement between the spatial distributions of the ^{13}CO and C^{18}O emission, and between the C^{18}O and H^{13}CO$^+$ emission in each velocity channel. Note that the peak position of the C^{18}O emission does not coincide with the H^{13}CO$^+$ peak in the GF 9-2 core (see $V_{\rm LSR} = -2.7$ and -2.5 km s^{-1} panels in Figure 4b). Fourth, the ^{13}CO channel maps show that, in addition to the Component 1, there exists another spatially coherent structure in the southern parts of the velocity panels of $-2.1 \lesssim V_{\rm LSR}/{\rm km\ s^{-1}} \le -0.7$. This structure, "Component 2", is elongated along the southeast-northwest direction, and shows intense ^{13}CO emission towards the south-east. Its local maxima is found at the bottom left corners of the velocity channels of $V_{\rm LSR} = -2.1$ and -1.9 km s^{-1} (Figure 3). For the C^{18}O line, the Component 2 is mainly identified in the panels of $-2.3 \lesssim V_{\rm LSR}/{\rm km\ s^{-1}} \le -1.7$. Last, the gas seen in the $V_{\rm LSR} = -2.3$ km s^{-1} panel is highly likely emanated from the two components. Despite the fact that the two components are not well separable in the velocity space, we define the boundary velocity between the dual components as -2.2 km s^{-1} in $V_{\rm LSR}$. This is because the C^{18}O emission associated with the GF 9-2 core is not recognized in the channel maps redward of $V_{\rm LSR} \gtrsim -2.1$ km s^{-1} (Figure 4a).

Since we detected significant ^{13}CO emission to the south-west of the core (e.g., Figure 2b), we compared two

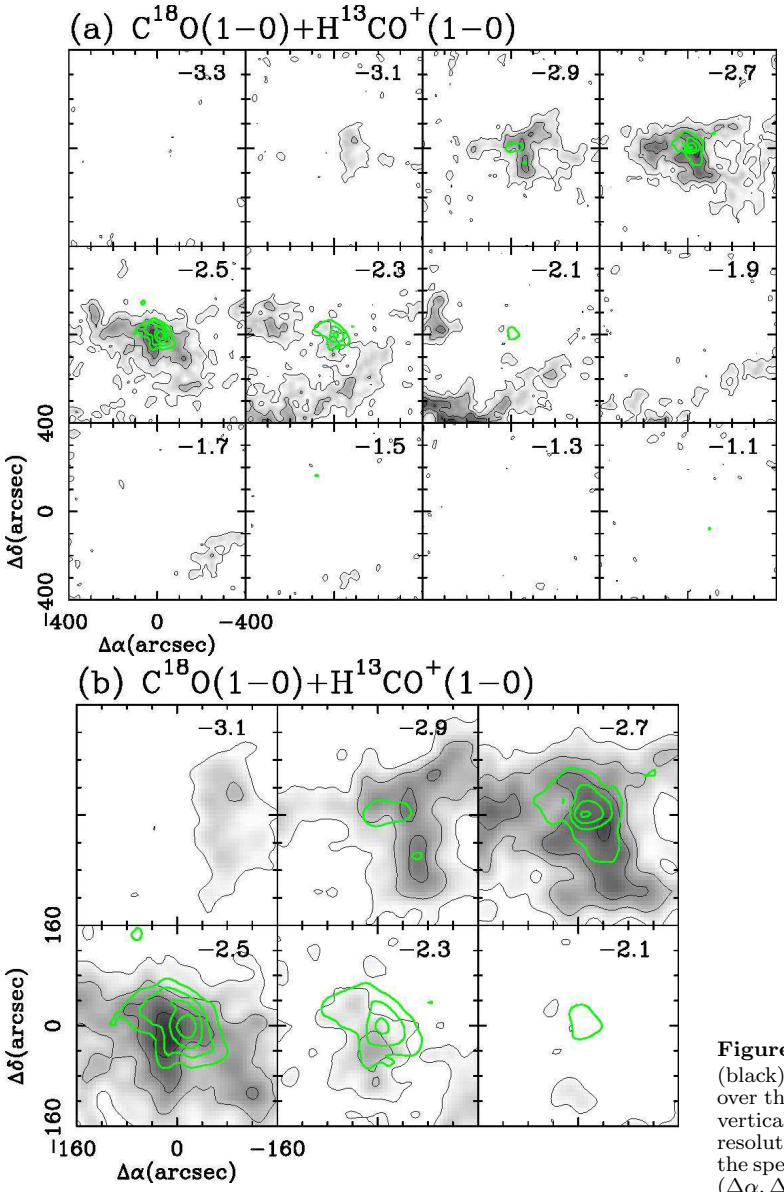

Figure 4. Velocity channel maps of the $C^{18}O$ (1–0) (greyscale plus black contours) and $H^{13}CO^+$ (1–0) (green contours) emission for (a) whole the observed area and (b) the central $320'' \times 320''$ region. The $H^{13}CO^+$ line data are taken from paper I. All the contours are plotted at 3σ intervals starting from the 3σ levels where σ = 100 mK and 220 mK in $T_{\rm mb}$ for the $C^{18}O$, and $H^{13}CO^+$ lines, respectively. Each channel map is averaged over a 0.2 km s^{-1} bin whose central LSR-velocity is shown in unit of km s^{-1} at the top right corner of each panel.

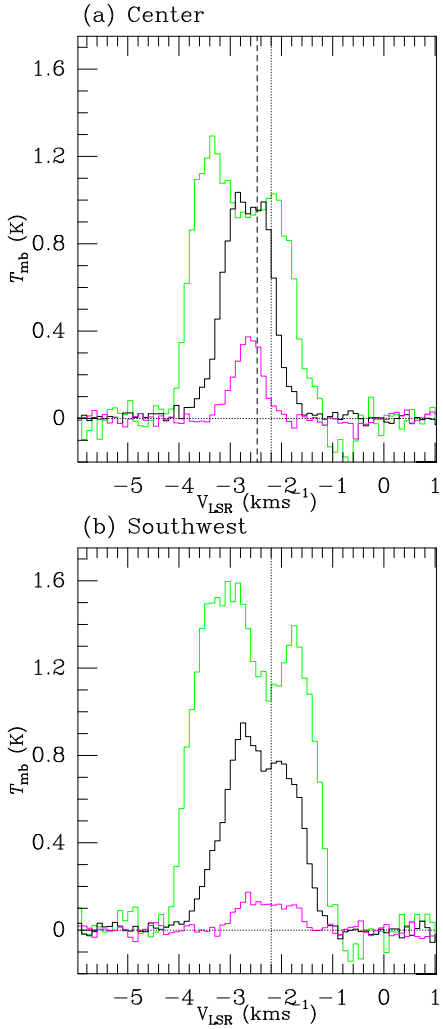

Figure 5. Spectra of the J = 1–0 lines of the ^{12}CO (green), ^{13}CO (black), and $C^{18}O$ (magenta) obtained by averaging the emission over the two circles with a $100''$ radius shown in Figure 2a - c. The vertical scale is the $T_{\rm mb}$ in K the same as in Figure 1. Velocity resolutions of the spectra are 0.1 km s^{-1}. The panel (a) represents the spectra towards the core center while the panel (b) does those at $(\Delta\alpha, \Delta\delta) = (-250'', -150'')$ with respect to the 3 mm continuum position. The vertical dashed line at $V_{\rm LSR} = -2.48$ km s^{-1} in the panel (a) shows the systemic velocity of the cloud ($V_{\rm sys}$; paper I), and the vertical dotted lines in the two panels indicate $V_{\rm LSR} = -2.2$ km s^{-1} which is the velocity boundary between the two gas components (see §4.3).

spectra obtained towards the core and the south-western region (Figure 5). These spectra were obtained by averaging the emission inside the circles shown in Figures 2a - 2c. Figure 5 shows the following features: (i) the ^{12}CO emission in the south-west is stronger than in the center, (ii) a comparison between the two ^{13}CO spectra suggests that dividing the filament gas into the two components by $V_{\rm LSR} = -2.2$ km s^{-1} seems to be reasonable, (iii) the $C^{18}O$ emission towards the core is approximately twice as intense as the emission towards the south-west, and (iv) towards the core center, the LSR-velocity of the $C^{18}O$ peak agrees with those of the central dips seen in the ^{12}CO and ^{13}CO spectra (Figure 5a). However these LSR-velocities are shifted by ~ -0.2 km s^{-1} with respect to the $V_{\rm sys}$.

We show the two integrated intensity maps of the Components 1 and 2 in Figure 6 by adopting $V_{\rm LSR}$= −2.2 km s^{-1} as the boundary velocity. The ^{13}CO emission in the velocity range of $-4.0 \leq V_{\rm LSR}/{\rm km\ s^{-1}} \leq -2.2$ (Figure 6a) is clearly associated with the dense core gas, which reconciles with the fact that the $C^{18}O$ emission seen in each panel center of $-3.2 \leq V_{\rm LSR}/{\rm km\ s^{-1}} \lesssim -2.2$ (Figure 4a) is predominantly associated with the core. In contrast, the ^{13}CO gas in Figure 6b is not associated with the dense core. As seen in the $V_{\rm LSR}$= −2.3 km s^{-1} pan-

els of Figures 3 and 4a as well as the spectrum in Figure 5b, it is impossible to separate completely the two components. We consider that they are partially overlapping in the line-of-sight and, and are partially interacting with each other. In §4 we analyze the data by showing their boundary, instead of separating them.

4. ANALYSIS

4.1. *Producing Opacity-Corrected ^{13}CO $J = 1 - 0$ Spectra*

In order to discuss the velocity structure of the filament gas, we corrected the cube data for the line broadening due to optical thickness (e.g., Phillips et al. 1979), and made opacity-corrected ^{13}CO spectra. This required us to estimate velocity width of the ^{13}CO line in the limit of $\tau \to 0$, $\Delta v(\tau \to 0)$, where τ denotes the ^{13}CO optical depth. The choice of the ^{13}CO is due to the large optical depth of the ^{12}CO emission, and due to the absence of the C^{18}O emission in the low density region of the filament. As described in Appendices A.1 and A.2, we utilized the three CO isotopologues to estimate the optical depth and excitation temperature ($T_{\rm ex}$) of the ^{13}CO line. We multiplied a factor of $\tau/(1 - e^{-\tau})$ to the observed $T_{\rm mb}$ of the ^{13}CO line to obtain the opacity-corrected $T_{\rm mb}^{\rm corr}$ at each LSR-velocity [see Eq.(A10) in Appendix A.4]. After obtaining the opacity-free spectrum such as shown in Figure 18e, we generated a 3D data cube by keeping the effective spatial resolution of 24.″0 and the velocity resolution of 0.1 km s^{-1} (§2). The opacity-free ^{13}CO cube data were analyzed as described in the subsequent subsections, and our usage of the ^{12}CO and C^{18}O line data are limited to estimating τ and $T_{\rm ex}$ of the ^{13}CO emission.

4.2. *Maps of Optical Depth and Excitation Temperature*

Figures 7 and 8 present velocity channel maps of the $\tau_{^{13}\rm CO}$ and $T_{\rm ex}$ of the ^{13}CO (1–0) line emission, respectively. Because of our 3σ level detection threshold (Appendix A.2) and the quality assessment of the results (Appendix D), we have no data points blueward of the $V_{\rm LSR}$= −3.7 km s^{-1} channel and redward of the $V_{\rm LSR}$= −1.1 km s^{-1} channel where the weak ^{13}CO emission is seen in Figure 3. Figure 7 shows that the ^{13}CO emission is moderately opaque with $\tau_{^{13}\rm CO} \sim 1$ in the ambient regions, and becomes optically thick towards the core. We measure a mean $\tau_{^{13}\rm CO}$ of 0.78±0.32 and a mean $T_{\rm ex}$ of 8.4±1.0 K for all the data shown in Figures 7 and 8, respectively.

Towards the position of the dense core, we have τ and $T_{\rm ex}$ estimates blueward of $V_{\rm LSR} = -2.3$ km s^{-1}, but no estimates redward of $V_{\rm LSR}$= −2.1 km s^{-1}. The highest optical depth in the GF 9-2 core region is measured at the local peak of 5.8±0.9 at $V_{\rm LSR}$= −2.7 km s^{-1}, leading to the C^{18}O optical depth of 1.1 with the solar abundance ratio of [^{13}CO]/[C^{18}O] = 5.5. We measure a mean $\tau_{^{13}\rm CO}$ of 1.31±0.30 and a mean $T_{\rm ex}$ of 8.0±0.7 K for the region enclosed by the 3σ level contour of the H^{13}CO$^+$ emission. Inside the 50% intensity contour with respect to the peak intensity for the N_2H^+ (1–0) emission (paper I), a mean $T_{\rm ex}$ is calculated to be 7.9±0.6 K which agrees with the $T_{\rm ex}$ = 9.5±1.9 K derived from the N_2H^+ line in the previous work within the uncertainties. In addition, for a circular region with a radius of 0.1 pc centered on the GF 9-2 core, we measure a mean $T_{\rm ex}$ of 8.0±0.1 K

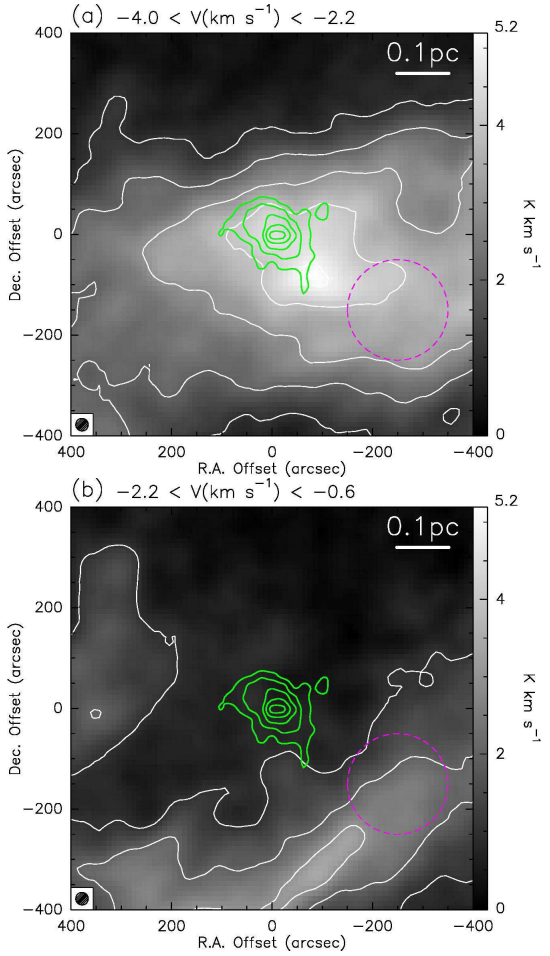

Figure 6. Integrated intensity maps of the ^{13}CO J =1–0 emission in the unit of K·km s^{-1}. The maps in panels (a) and (b) are integrated the emission in $T_{\rm mb}$ over the LSR-velocity ranges of $-4.0 \leq V_{\rm LSR}/{\rm km\ s^{-1}} \leq -2.2$ and $-2.2 \leq V_{\rm LSR}/{\rm km\ s^{-1}} \leq -0.6$, respectively (see Figure 5). Note that the intensity ranges in the two maps are the same. The white contours have the intervals of 1.0 K·km s^{-1} starting from the 1.0 K·km s^{-1} level which corresponds to the 12σ and 8σ levels in the maps (a) and (b), respectively. The peak intensity of 5.2 K·km s^{-1} in the panel (a) is found at $(\Delta\alpha, \Delta\delta) = (-76'', -78'')$ with respect to the 3 mm source position, while that of (b) (3.4 K·km s^{-1}) was measured at $(-86'', -326'')$. The green contours show the H^{13}CO$^+$ total map in the same fashion as for Figure 2. The magenta dashed circles show the area where the CO isotopologue emission are integrated to obtain the spectra shown in Figure 5b.

which agrees with the $T_{\rm ex}$ value expected from the Monte Carlo simulation by Ciardi et al. (2000) (see their Figure 9). In conclusion, the calculated $T_{\rm ex}$ velocity channel maps have reasonable consistency with the previous results. Assuming that the gas is in LTE, we consider that the $T_{\rm ex}$ represents the kinetic temperature ($T_{\rm kin}$) of the gas.

In Figure 8, we found regions where $T_{\rm ex}$ is elevated up to $\sim$ 14 K to the south-west of the core in the $V_{\rm LSR}$= $-2.9 \sim -2.5$ km s^{-1} panels and the −1.7 km s^{-1} one, which belong to the Components 1 and 2, respectively. It is also interesting that the velocity channels between them (i.e., $-2.3 \leq V_{\rm LSR}/{\rm km\ s^{-1}} \leq -1.9$) do not have such high temperature regions. These features will be discussed in §5.5.2.

In order to calculate the column density of the ^{13}CO

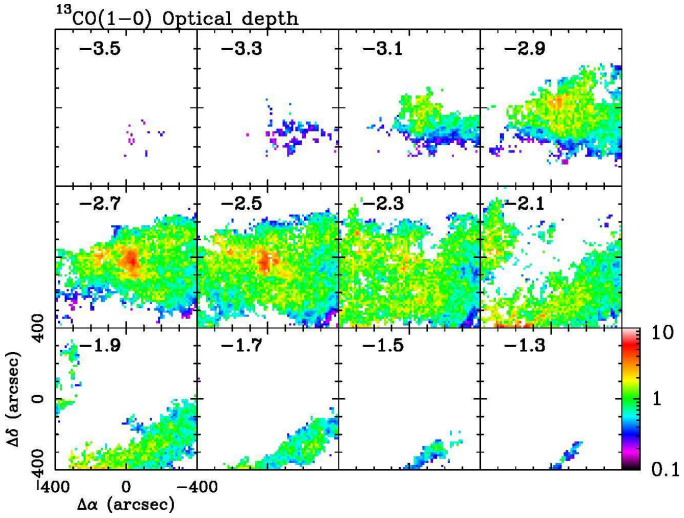

Figure 7. Velocity channel maps of the optical depth of the ^{13}CO (1–0) emission with velocity intervals of 0.2 km s^{-1}. The central LSR-velocity of each channel in km s^{-1} is shown at the top left corner of each panel. The optical thickness is shown in logarithmic scale (see the color bar). The maximum optical depth of 10.0±3.2 is measured near the southern edge of the $V_{\rm LSR}$ = −2.1 km s^{-1} panel, while the second highest value of 5.8±0.9 was measured towards the GF 9-2 core at $V_{\rm LSR}$ = −2.7 km s^{-1}.

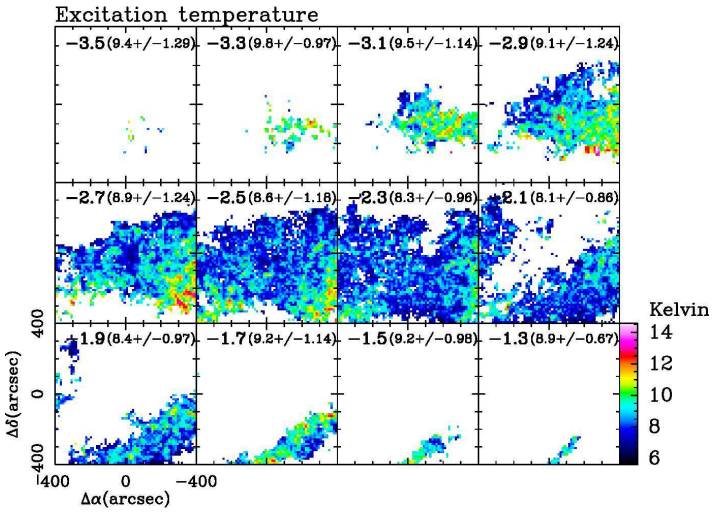

Figure 8. Velocity channel maps of the excitation temperature of the ^{13}CO (1–0) emission in K with velocity resolution of 0.2 km s^{-1}. The central LSR-velocity of each velocity channel in km s^{-1} is shown at the top left corner of each panel. The two numbers in the parenthesis with the +/- sign indicate the mean and standard deviation of the excitation temperature in each panel in unit of K. Notice that the excitation temperature is shown in linear scale (see the color bar).

molecules, we subsequently produced a mean $T_{\rm ex}$, $\langle T_{\rm ex}\rangle$, map from the $T_{\rm ex}$ data cube. The $\langle T_{\rm ex}\rangle$ map is shown in Figure 9. We averaged $T_{\rm ex}(v)$ values along the velocity axis where the $T_{\rm mb}^{\rm corr}(v)$ intensities exceed our detection threshold of the 3σ level (see Figures 18d and 18e). We obtained the mean value for $\langle T_{\rm ex}\rangle$ of 7.5±1.0 K over the presented region, and adopted this value as the representative $T_{\rm kin}$ for the region.

4.3. *Maps of Total Intensity, Centroid Velocity, and Velocity Width*

The color images in Figure 10 represent total integrated intensity, intensity-weighted mean velocity, i.e., centroid velocity ($v_{\rm cent}$), and velocity width (FWHM) maps produced from the opacity-corrected ^{13}CO spectra. After calculating the zeroth, first, and second order moments as well as their errors at each spatial position, we produced the maps without any smoothing (Appendices B and D). Since we are interested in the natal cloud of the dense core, we indicate the boundary between the Components 1 and 2 by the black-in-white contours which correspond to $v_{\rm cent}$ = −2.2 km s^{-1} in Figure 10b.

Figure 10a shows us that the morphology of the ^{13}CO bright region is principally similar to the distribution of the C^{18}O emission (Figures 2c and 2f), and that the dense core traced by the H^{13}CO$^+$ emission has formed in the inner densest part of the filamentary cloud. Figure 10b shows that the Component 1 gas is confined in a narrow velocity range of ∼0.6 km s^{-1} ($-2.8 \lesssim v_{\rm cent}/{\rm km\ s^{-1}} \lesssim -2.2$) which is about twice the isothermal sound velocity ($c_{\rm s}^2 = 8\ln 2\,\frac{kT_{\rm kin}}{\mu m_{\rm H}}$ where μ denotes the mean molecular weight of 2.33 for [He] = 0.1 [H]). The measured $v_{\rm cent}$ of the immediate surroundings of the dense core shown in the blue-to-dark magenta (corresponding to $-2.8 \lesssim v_{\rm cent}/{\rm km\ s^{-1}} \lesssim -2.6$) has reasonable consistency with the velocity structure of the dense core traced by the H^{13}CO$^+$ (1–0) and N_2H^+ (1–0) line observations (see Figure 12 in paper I). As we argued in §3 with Figures 5 and 6, the two gas components cannot be separated completely, Figure 10b demonstrates that the main body of the Component 2 gas is seen in $V_{\rm LSR} \gtrsim -2$ km s^{-1}. Another important result from Figure 10b is that neither systematic motions of the gas caused by any activities of YSOs, such as a well-collimated typical molecular outflow, nor any sharp discontinuity of the line-of-sight velocity, e.g., due to shock fronts, can be recognized. These velocity features strongly suggest that both the Components 1 and 2 belong to the GF 9 filament (Schneider & Elmegreen 1979) where seven dense cores and three possible candidates are located at regular intervals of ∼0.9 pc (paper II).

Figure 10c shows that the velocity width is enhanced up to ∼ 1.4 km s^{-1} in the fourth quadrant of the map. The extent of this region is almost the same as the south-western intensity enhancement seen in Figure 10a. The mean velocity width for the fourth quadrant is $\Delta v_{\rm FWHM}$ = 0.96±0.24 km s^{-1}, while the mean value for the first to third quadrants is 0.69±0.12 km s^{-1}. Both the mean values exceed the isothermal sound velocity width in FWHM of 0.38±0.13 km s^{-1} for $T_{\rm kin}$ = 7.5±1.0 K (§4.2).

4.4. *Column Density Map and LTE Mass*

After obtaining the maps of the total integrated intensity, $\int T_{\rm mb}^{\rm corr}(v)dv$ (Figure 10a), and the mean excitation temperature $\langle T_{\rm ex}\rangle$ (Figure 9), one can readily calculate ^{13}CO column density, $N_{^{13}{\rm CO}}$ (Appendix C). Here we used the $\langle T_{\rm ex}\rangle$ map (Figure 9) instead of the $T_{\rm ex}$ channel maps (Figure 8). Considering the $T_{\rm ex}$ range of $5.6 \le T_{\rm ex}/{\rm K} \le 13.6$ (see Figure 8), the dependency of $T_{\rm ex}$ in the $N_{^{13}{\rm CO}}$ calculations is smaller than the other errors

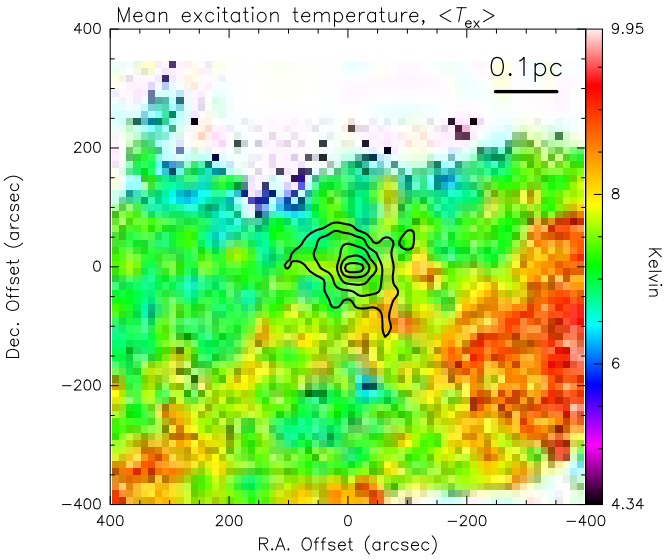

Figure 9. Plot of mean excitation temperature obtained by averaging the $T_{\rm ex}(v)$ spectra at each pixel position across the velocity axis (see Figure 8). The contours represent the total map of the $H^{13}CO^+$ (1–0) emission in the same manner as for Figure 2. The 0.1 pc scale is indicated at the top right corner, and the color bar is on the right-hand side of the panel.

[see Eqs.(C1) and (C2) in Appendix C]. Furthermore, the $T_{\rm ex}(v)$ spectra are generally "flat" with respect to the LSR-velocity (see Figure 18d), justifying the usage of the $\langle T_{\rm ex}\rangle$ value as the representative $T_{\rm ex}$ at each map pixel.

Figure 11 presents a map of the molecular hydrogen column density ($N_{\rm H_2}$) that is converted from the ^{13}CO column density by adopting the ^{13}CO fractional abundance of $X(^{13}{\rm CO}) = 2\times10^{-6}$ (e.g., Dickman 1978; Frerking et al. 1982; Lequeux 2005). The $N_{\rm H_2}$ map clearly demonstrates that the filament has a high-column density region in the center where the $H^{13}CO^+$ core is observed. In addition, the map also shows that the filament gas has a column density range of $20.7 \lesssim \log N_{\rm H_2}/{\rm cm^{-2}} \lesssim 21.8$. We measure a mean $N_{\rm H_2}$ of $(2.7\pm0.9)\times10^{21}$ cm^{-2} for the Component 1 and $(2.4\pm0.7)\times10^{21}$ cm^{-2} for the Component 2. We calculate LTE-masses ($M_{\rm LTE}$) of 24 ± 10 $M_\odot$ and 17 ± 7 $M_\odot$ for the Components 1 and 2, respectively, with $d=200$ pc.

We checked consistency with the previous work by Ciardi et al. (2000). We measured the maximum $N_{^{13}{\rm CO}}$ of 1.2×10^{16} cm^{-2} at the center of the GF 9-2 core. This agrees with the value that can be read from Figure 6a in Ciardi et al. (2000) (1.4×10^{16} cm^{-2}). It should be noted that Ciardi et al. (2000) used $d=440$ pc, and estimated $M_{\rm LTE}$ of 53 ± 8 $M_\odot$ for a rectangular region of $480''\times600''$ centered on the GF 9-2 core. Towards the same rectangle, we measured a mean $N_{^{13}{\rm CO}}$ of $(5.3\pm2.2)\times10^{15}$ cm^{-2}. With $d=440$ pc, we recalculated $M_{\rm LTE}$ of 55 ± 23 $M_\odot$ from the mean $N_{^{13}{\rm CO}}$. Therefore our analysis with $d=200$ pc has good consistency with the previous one with $d=440$ pc.

A hint to discuss the origin and nature of the filament may be obtained from a histogram of the H_2 column density and its cumulative distribution shown in Figure 12. The histogram is well approximated

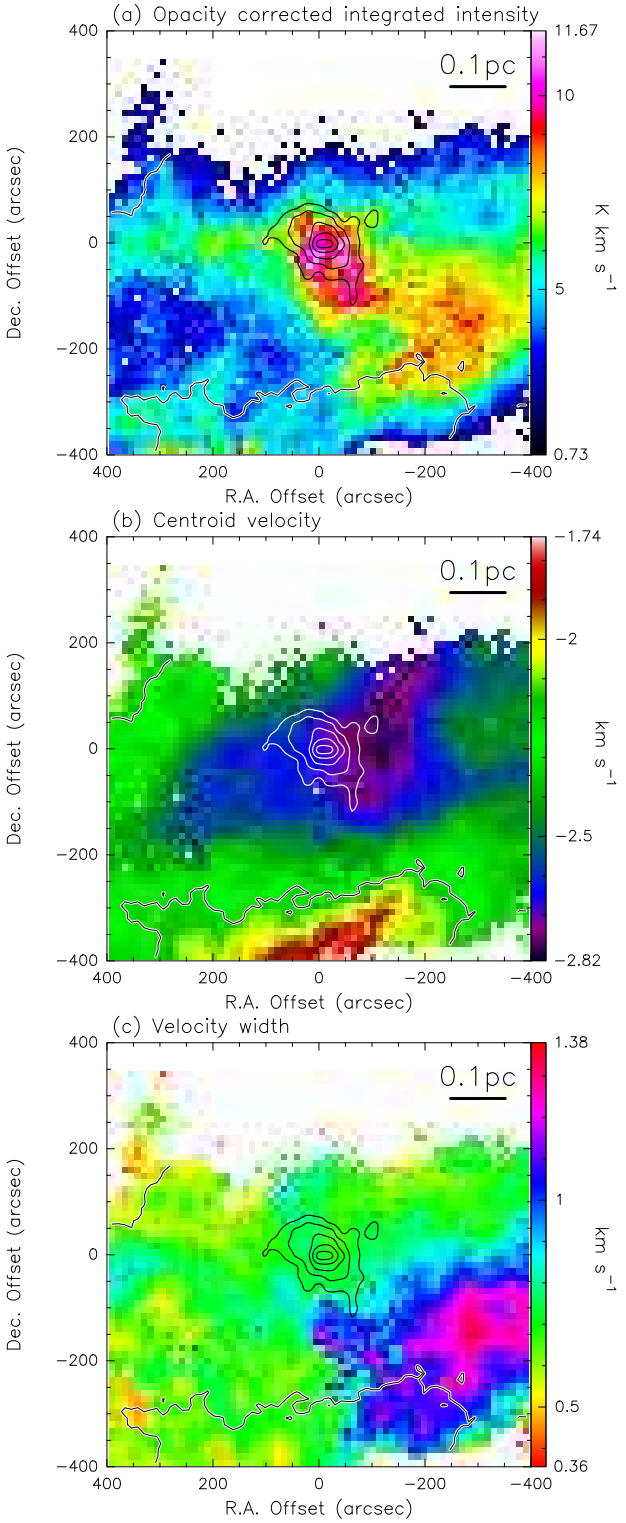

Figure 10. Maps of (a) the total intensity in K km s^{-1}, (b) centroid velocity in km s^{-1}, and (c) velocity width (FWHM) in km s^{-1} produced from the opacity-corrected ^{13}CO (1–0) spectra (§4.1). The pixel sizes of these maps are 12″, i.e., half of the effective beam size (§2). The color bar on the right-hand side of each plot shows the plotted range in linear scale. The 0.1 pc-scale at the distance of 200 pc is shown at the top right corner of each panel. The contours at each map center represent the $H^{13}CO^+$ total map as shown in Figure 2. The black-in-white contours seen in the south and the north-east of the panel (b) represent the $v_{\rm cent} = -2.2$ km s^{-1} contours which are also shown in the panels (a) and (c). See §3 for the reasoning.

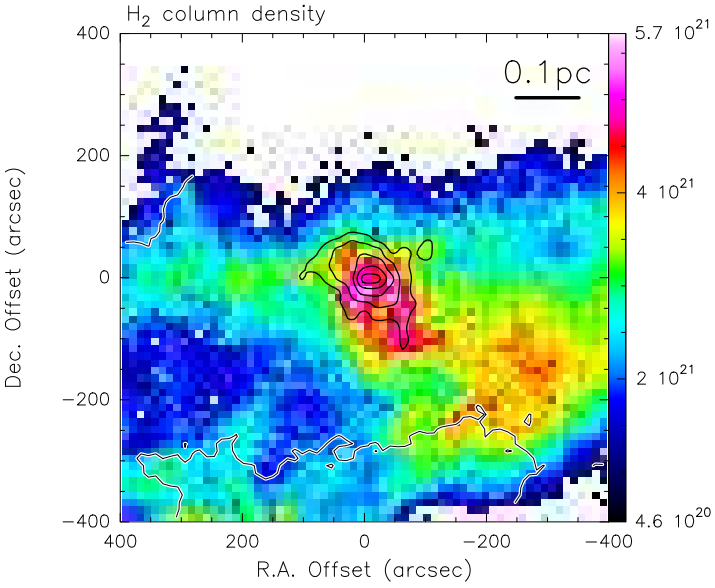

Figure 11. Map of the total column density of molecular hydrogen ($N_{\rm H_2}$) derived from the ^{13}CO emission in unit of cm^{-2}. The color scale is shown in logarithmic as shown in the color bar. The 0.1 pc scale is indicated at the top right corner. The black contours at the center represent the H^{13}CO$^+$ total map as shown in Figure 2. The black-in-white contours in the south and the north-east of the core correspond to the $v_{\rm cent} = -2.2$ km s^{-1} contours as shown in Figure 10.

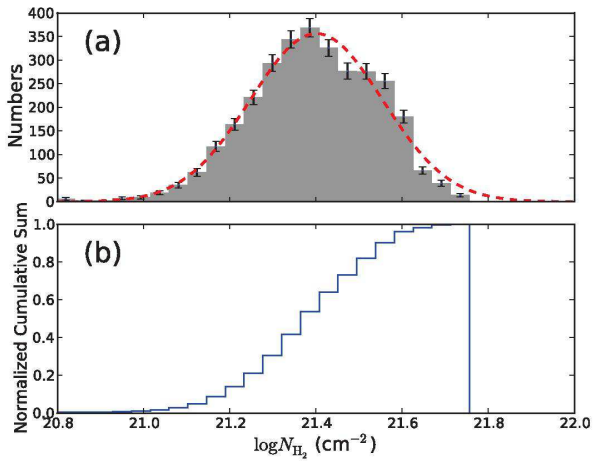

Figure 12. (a) Histogram of the molecular hydrogen column densities ($N_{\rm H_2}$) shown in Figure 11. The dashed red curve indicates the best-fit log-normal function with a mean of 21.4, i.e., 2.52×10^{21} cm^{-2} (corresponding to the 50% percentile in the panel b) and a standard deviation of 0.15. (b) Plot of normalized cumulative sum calculated from the histogram.

by a log-normal probability distribution function with a standard deviation of 0.15, indicating that the turbulence formed the density structure of the filament gas (see e.g., Ostriker et al. 2001; Padoan & Nordlund 2002; Ossenkopf & Mac Low 2002; Nakamura & Li 2007; Kainulainen et al. 2009). In addition, Figure 12b shows that 50% of the filament materials exist in the higher column density region of $N_{\rm H_2} \gtrsim 2.5 \times 10^{21}$ cm^{-2}, which is similar to the results obtained in Taurus (Goldsmith et al. 2008). The order of the derived column density ($N_{\rm H_2} \sim 10^{21}$ cm^{-2}) corresponds to the visual extinction of $A_{\rm v} \sim 1$ which is comparable to those measured from the optical images (Schneider & Elmegreen 1979; Poidevin & Bastien 2006).

5. DISCUSSION

In this section, we discuss the nature of the filament gas to shed light on the initial conditions of the dynamical collapse of the GF 9-2 cloud core which harbors the exceptionally young low-mass protostar (papers I and III). On the basis of all the results and analysis, we conclude that the core is physically associated with the Component 1 filament (§3 and §4.3). This is because the dense core is located at the local density maxima of the Component 1 and the LSR-velocity of the core falls in the velocity range of the Component 1. Although it is impossible to separate the two components completely, the Component 2 is not the natal gas of the GF 9-2 core.

5.1. *Turbulent Motions of the Gas in the Component 1*

We present a map of the ratio between the non-thermal velocity dispersion ($\sigma_{\rm nth}$) and the sound velocity $c_{\rm s}$ in Figure 13 to examine the degree of turbulence in the Component 1. The ratio is obtained from,

$$\left(\frac{\sigma_{\rm nth}}{c_{\rm s}}\right)^2 = \left\{\frac{\Delta v(\tau\rightarrow 0)}{c_{\rm s}\sqrt{8\ln 2}}\right\}^2 - \left(\frac{\sigma_{\rm thm}}{c_{\rm s}}\right)^2, \quad (1)$$

where $\sigma^2_{\rm thm}$ is given by $\frac{kT_k}{m_{^{13}\rm CO}}$, and $m_{^{13}\rm CO}$ denotes the molecular mass of ^{13}CO. For calculations of $\sigma_{\rm thm}$, we used the $\langle T_{\rm ex}\rangle$ map (Figure 9). Over the Component 1, we obtained a mean ratio of $\langle\sigma_{\rm nth}/c_{\rm s}\rangle = 2.1\pm0.50$, corresponding to $\langle\sigma_{\rm nth}\rangle = 0.34\pm0.080$ km s^{-1}. The observed non-thermal contribution must be simply attributed to the random turbulent motions of the gas because we did not identify any systematic motions of the filament gas (§4.3).

In the following, we deal with the Component 1 as a single filament, and we do not consider an interpretation proposed by Hacar & Tafalla (2011) that a supersonic turbulent filament is mimicked by "twisted" subsonic filaments. In summary, the internal motion of the filament gas is governed by the supersonic turbulence. Note that our conclusion differs from that by Poidevin & Bastien (2006) who inferred the absence of turbulence in the filament based on their polarization maps.

5.2. *Is the Component 1 Radially Supported by the Supersonic Turbulence?*

Next we assess whether or not the filament is dynamically supported by the supersonic turbulence against radial collapse. This yields the first step to discuss how the gravitational collapse of the GF 9-2 core (paper I) was triggered in the supersonic turbulent filament. For this purpose, we examine the stability of the Component 1 gas based on a model for an isothermal cylinder in hydrostatic equilibrium (Stodólkiewicz 1963; Ostriker 1964). Although the mean $T_{\rm ex}$ map shows that the gas temperature in the south-western region is enhanced up to $\sim$ 10 K (Figure 9), we assume that the filament is isothermal with 7.5 K (§4.3) as the first order of approximation. The model gives the radial density distribution

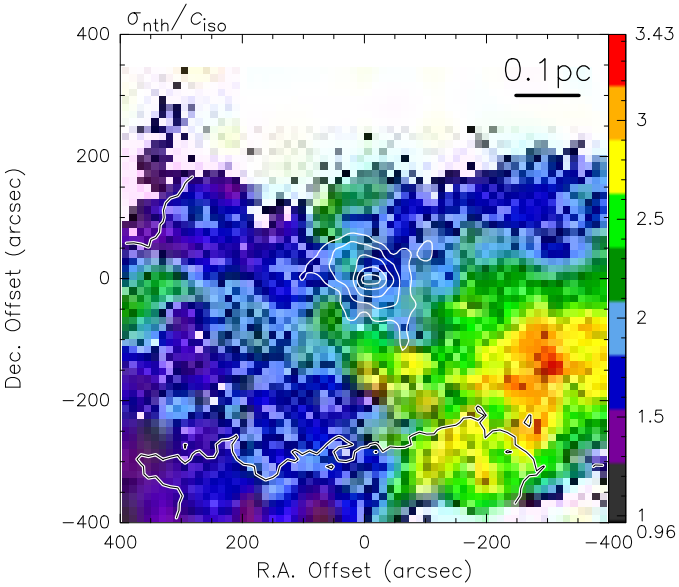

Figure 13. Map of the ratio between the non-thermal velocity dispersion and the local sound speed. See §5.1 for details. The color bar shows the ratio in linear scale. The 0.1-pc scale at the distance of 200 pc is shown at the top right corner of the panel. The white contours at the center represent the $H^{13}CO^+$ total map as shown in Figure 2, and the black-in-white contours in the south and the north-east of the core indicate the $v_{\rm cent} = -2.2$ km s^{-1} contours as in shown Figure 10.

of,

$$\rho(\bar{\omega}) = \rho_{\rm c}\left\{1+\left(\frac{\bar{\omega}}{H}\right)^2\right\}^{-2}. \quad (2)$$

Here $\bar{\omega}$ is the radial distance from the cylinder axis, and H is the scale height given by,

$$H = \sqrt{\frac{2c_{\rm s}^2}{\pi G\rho_{\rm c}}} \sim \lambda_{\rm J}, \quad (3)$$

where $\rho_{\rm c}$ is the central density of the filament and $\lambda_{\rm J}$ the Jeans length at $\rho_{\rm c}$. Therefore, the critical line mass ($m_{\rm line,crit}$), above which the cylinder radially collapses, is calculated by,

$$m_{\rm line,crit} = \int_0^\infty 2\pi\bar{\omega}\rho(\bar{\omega})d\bar{\omega} = \frac{2c_{\rm s}^2}{G}, \quad (4)$$

which does not depend on $\rho_{\rm c}$. To apply this model to the Component 1 where the supersonic turbulence dominates the gas kinematics, we replace $c_{\rm s}^2$ with $c_{\rm s}^2+\sigma_{\rm nth}^2$, and define an *effective critical line-mass* by,

$$m_{\rm line,crit}^{\rm eff} = \frac{2}{G}\frac{kT_{\rm kin}}{\mu m_{\rm H}}\left\{1+\left(\frac{\sigma_{\rm nth}}{c_{\rm s}}\right)^2\right\}. \quad (5)$$

This equation represents the maximum *line-mass* that can be supported by the total internal pressure of the filament. We stress that the $\sigma_{\rm nth}$ term represents the non-thermal pressures due to predominantly the supersonic turbulence (§5.1) and probably the magnetic field as well (described in §5.4), although it is impossible to separate them. Using $\langle T_{\rm kin}\rangle = 7.5\pm1.0$ K (§4.3) and $\langle\sigma_{\rm nth}/c_{\rm s}\rangle = 2.1\pm0.50$ (§5.1), we calculated an effective critical mass ($M_{\rm crit}^{\rm eff}$) of 51^{+32}_{-22} $M_\odot$ for the Component 1 by multiplying $m_{\rm line,crit}^{\rm eff}$ of 41^{+35}_{-26} $M_\odot$ pc^{-1} by the observed length of the filament (0.77 pc; see Figure 2). Comparing the $M_{\rm crit}^{\rm eff}$ value to the $M_{\rm LTE}$ of 24 ± 10 $M_\odot$ (§4.4), we suggest that the filament is highly likely gravitationally stable with respect to radial collapse owing to the turbulent support. Note that the filament cannot be supported only by the thermal pressure because the LTE mass is larger than $m_{\rm line,crit}\times0.77\,{\rm pc}\sim9$ $M_\odot$ [see Eq.(4)].

5.3. *Does the Component 1 Fragment Axially?*

5.3.1. *Estimate of the Filament Scale Height from the Column Density Map*

To discuss the axial fragmentation of the Component 1, we estimated the scale height of the filament from the column density map (Figure 11) using the Stodolkiewicz-Ostriker model (§5.2). A column density profile of an isothermal cylinder supported by the thermal and turbulent pressures can be written from Eq.(2) as,

$$N_{\rm H_2}(r) = \frac{c_{\rm s}^2+\sigma_{\rm nth}^2}{\mu m_{\rm H}GH}\left\{1+\left(\frac{r}{H}\right)^2\right\}^{-\frac{3}{2}}, \quad (6)$$

where r is the projected distance from the central axis of the cylinder in the plane of the sky. We applied this equation to the Component 1 gas in the column density map (Figure 11). In the model fitting we adopted P.A. $= -90°$ for the cylinder axis, which was forced to pass the position of the 3 mm continuum source, and $\langle\sigma_{\rm nth}\rangle = 2.1c_{\rm s} = 0.34$ km s^{-1}, setting only H as a free parameter. This is because we could not well determine the P.A. value and the location of the central axis as free parameters owing to the insufficient spatial coverage of the observations.

Figure 14 presents maps of the column density, the best-fit model, and the residual for the Component 1. Figure 15 shows the radial profile of the column density averaged along the R.A. direction, and we obtained the best-fit value of $H = 0.68\pm0.04$ pc by considering the uncertainty in the column density (see Appendices C and E). We notice that the derived width of $2H = 1.4$ pc is significantly larger than the observed width of the filament of $\sim600''$ (see e.g., Figure 10), corresponding to 0.58 pc. Our analysis may be also affected by the small dynamic range of the column density of $20.9\lesssim\log N_{\rm H_2}/{\rm cm}^2\lesssim20.8$ (Figures 11 and 12) and possibly by the asymmetric structure of the filament (see Figure 15) which exists all over the observed region. If we underestimated the peak column density, then the H value would become small according to Eq (6).

The best-fit H value leads to the filament width in FWHM to be $1.5H = 1.0\pm0.03$ pc which is significantly larger than the typical width of ~0.1 pc derived from the *Herschel* survey towards the IC 5146 (Arzoumanian et al. 2011) and B211/213 (Palmeirim et al. 2013) regions. In order to assess whether or not the difference is caused by that between the adopted models, we reanalyzed our column density map using the Plummer-like cylinder model (see e.g., Eq.(B1) in Palmeirim et al. 2013, and references therein) instead of using Eq.(6). Notice that the Plummer-like function (Plummer 1911; Nutter et al. 2008) has three free parameters, while the Stodolkiewicz-Ostriker-like cylinder that we adopted has only one, i.e., H. With the Plummer-like function we estimated the fil-

ament width in FWHM to be 0.38±0.06 pc, which is still significantly larger that those by *Herschel*. We therefore conclude that the difference between the *Herschel* filaments and the GF 9 one is real. One possible cause is that the CO lines in our study could not trace the higher density regions detected by the *Herschel* survey with the dust continuum emission. Alternative cause is that there might exist an intrinsic difference between the GF 9 and the regions that *Herschel* surveyed.

Considering all the results as well as their limitations, we adopt fiducial values of $H = 0.3 \sim 0.7$ pc for further discussion (Table 1). Here the lower limit of 0.3 pc is obtained from the map ($2H = 0.58$ pc) while the upper limit is from the best-fit value. The estimated range of the scale height leads to the ρ_c value in Eq.(2) of $(3 \sim 16) \times 10^{-21}$ g cm^{-3} using the relation in our model of,

$$\rho_c = \frac{2}{\pi G H^2} \left(c_{\rm s}^2 + \sigma_{\rm nth}^2\right). \quad (7)$$

The resultant ρ_c value corresponds to $n_{\rm c}({\rm H_2}) = 800 \sim 4200$ cm^{-3}which has reasonable consistency with the critical density required to excite the ^{13}CO $J = 1$–0 transition. It should be noticed that the above central density characterizes the tenuous filament gas surrounding the dense core GF 9-2 (not the dense core itself).

If the cylinder model is appropriate to the description of our data, a tenuous core-like structure is identified in the residual $N_{\rm H_2}$ map (Figure 14c). The position and extent of the "tenuous core" agree fairly well with those of the dense core observed in the N_2H^+ (1–0), $H^{13}CO^+$ (1–0), CCS $4_3 - 3_2$ and NH_3 (1,1) lines (paper I). We therefore speculate that it is a low-density envelope surrounding the dynamically infalling dense core (paper III). The LTE mass of the "tenuous core" is calculated to be $M_{\rm TEC} \sim 0.8\ M_\odot$ where TEC denotes the tenuous envelope of the core. Furthermore, we can estimate a "core formation efficiency" for the GF 9-2 dense cloud core of $\eta_{\rm CF} = M_{\rm LTE}/(M_{\rm LTE} + M_{\rm TEC}) = 1.3\ M_\odot/(1.3\ M_\odot + \sim 0.8 M_\odot) \gtrsim 60\%$ where $M_{\rm LTE}$ is the mass of the dense core traced by the N_2H^+ and $H^{13}CO^+$ lines (paper I).

5.3.2. *Gravitational Stability of the Component 1 against Axial Perturbations*

Theoretical studies by e.g., Nagasawa (1987) and Inutsuka & Miyama (1997) showed that the minimum wavelength ($\lambda_{\rm min}$) which makes an infinite filament unstable against perturbations along the major axis is given by $\lambda_{\rm min} \sim 4H$, regardless of the presence of the magnetic field along the axis [the definition of H in Nagasawa (1987) differs by $1/\sqrt{8}$ times of those in e.g., Inutsuka & Miyama (1992).]. The line mass of the filament can be calculated from the LTE-mass (§4.4) and the observed length as 24 $M_\odot$/ 0.77 pc = 31 $M_\odot$ pc^{-1}. Therefore the critical "clump mass" produced by the axial perturbation may be 31 $M_\odot$ pc^{-1} $\times\ 4H = 37 \sim 87$ $M_\odot$. It is clear that the estimated range of the clump masses is one order of magnitude larger than the LTE-masses of the NH_3 cores ($M_{\rm LTE} = 2 \sim 8\ M_\odot$: paper II). We therefore consider that the filament is gravitationally stable against the axial perturbations probably owing to the transverse magnetic field (Poidevin & Bastien 2006) which is reanalyzed in §5.4.

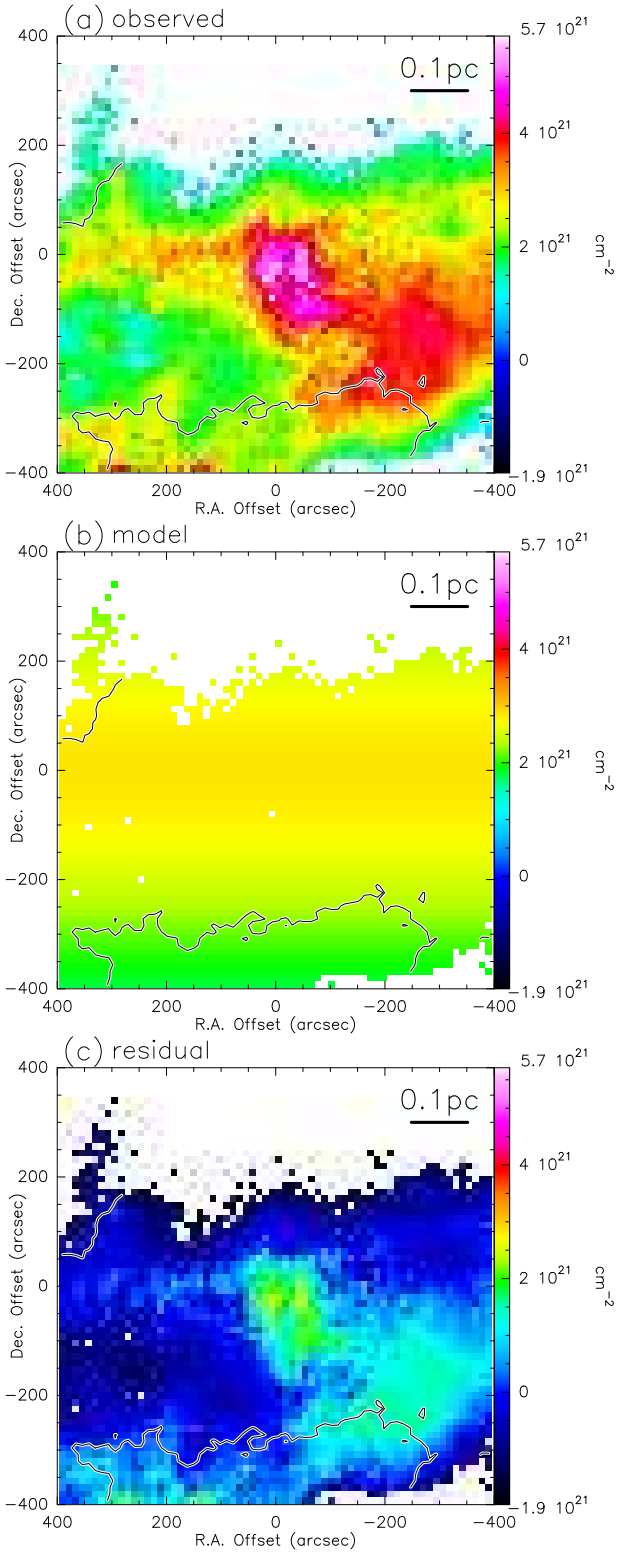

Figure 14. Model fitting to the molecular hydrogen column density of the Component 1. The panels (a), (b), and (c) show the observed column density (Figure 11), model, and residual maps, respectively. Note that all the color maps are shown in the fixed common range of the column density (see the color bars). See §5.2 for details.

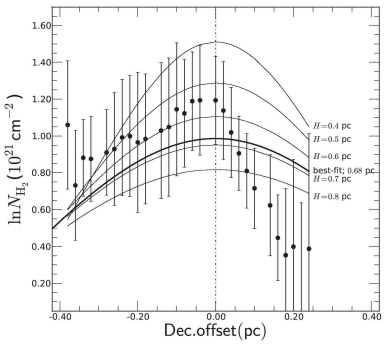

Figure 15. Radial column density profile of molecular hydrogen averaged along the central axis for the "Component 1" filament. The negative and positive sides of the Dec. offset axis, respectively, correspond to the south and north sides of the N_{H_2} map (Figure 14a). The thick curve presents the best-fit profile of the Stodolkiewicz-Ostriker cylinder model and the thin curves show the model profiles with the H values between 0.4 and 0.8 pc. See §5.3.1 and Appendix E.

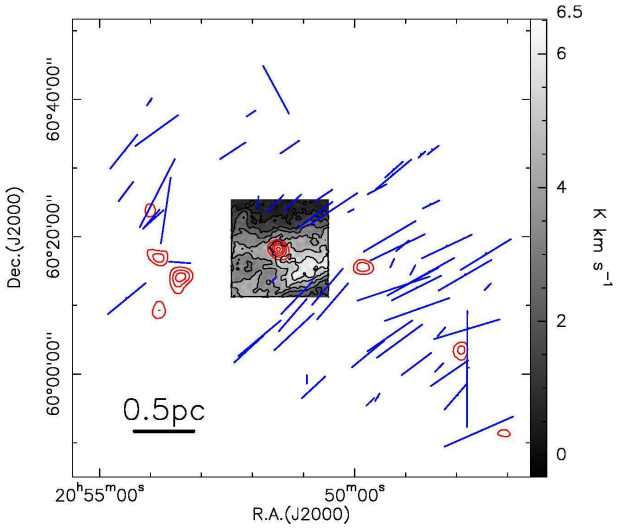

Figure 16. An overlay of the optical polarization map (blue line segments) plotted using the data shown in Table 1 of Poidevin & Bastien (2006) on the total integrated intensity maps of the NH_3 $(J,\ K)=(1,1)$ (red contours; paper II) and the ^{13}CO (1–0) (grey scale plus contours; see Figure 2a; starting from the 10σ level with the 10σ intervals) emission. The red contours start from the 6σ levels with the 3σ intervals as shown in paper II. The 0.5 pc scale is shown at the bottom left corner of the panel. The grey-scale bar at the right-hand side shows the integrated intensity of the inserted ^{13}CO map.

Alternatively, the GF 9 filament may have narrow subfilaments (Hacar & Tafalla 2011; Hacar et al. 2013) with $H \sim 0.1$ pc and $n_c \sim 10^4$ cm^{-3}. In fact, such a substructure may be recognized in the $C^{18}O$ total intensity map of Figure 2c. If this is the case, the axial fragmentation of the subfilament explains the observed spatial intervals of ∼0.9 pc between the NH_3 cores (paper II) because of (4–8)$H = 0.4 \sim 0.8$ pc. However, this scenario has a caveat that the expected "clump masses" given by $m^{\rm eff}_{\rm line,crit} \times$ (4–8) $H = 16 \sim 40\ M_\odot$ are larger than the LTE-masses of the NH_3 cores.

In summary, our analysis suggests that the natal gas of the core is in dynamical equilibrium with respect to both the radial and axial collapses. Naívely speaking, this inference does not seem to be reconciled with the presence of the dynamically collapsing core (papers I and III). Before resolving this issue, we assess the role of the large-scale magnetic field existing in the filament.

5.4. *Role of the Magnetic Field in the Gas Surrounding the GF 9-2 Cloud Core*

Figure 16 shows a comparison between the optical polarization map taken from Poidevin & Bastien (2006) and the distribution of the dense cores, including the candidates, seen in the NH_3 emission (paper II). Since the directions of the optical polarization angles are thought to be parallel to the magnetic field, Poidevin & Bastien (2006) pointed out that the magnetic field is almost perpendicular to the filamentary dark cloud (Schneider & Elmegreen 1979). Such a large-scale configuration is also found in the Taurus molecular cloud (see e.g., Chapman et al. 2011, and references therein) suggesting that the filament formed through compression of the diffuse gas by external pressure along the magnetic field or/and through gas accretion due to self-gravity along the magnetic field. However, this scenario should be reexamined in more detail because the optical polarization angles in the vicinity of the GF 9-2 core are inclined by ∼ 45° with respect to the Component 1 filament axis. It is also interesting that the polarization angles are almost parallel to the elongation of the Component 2 gas.

An alternative mechanism to produce such a large-scale configuration is that the observed field is the projected component of a toroidal field. Because of no firm evidence, we do not discuss this interpretation here. On the other hand, the magnetic field in the filament should be far from good alignment at small scales owing to micro-turbulence (e.g., White 1977; Heyer et al. 2008). However we can not discuss this issue because the angular resolution of the polarization map is too coarse to assess the role of the magnetic field at scales smaller than the core size of ∼0.1 pc.

It is well known that not only supersonic turbulence but also magnetic field prevent interstellar gas from collapsing due to its self-gravity. Applying the Chandrasekhar & Fermi method (Chandrasekhar & Fermi 1953a), Poidevin & Bastien (2006) estimated the magnetic field strength in the plane of the sky, $|\vec{B}_{\rm pos}|$. They derived $|\vec{B}_{\rm pos}|$ of $170 \pm 56\ \mu$G for the "Core" which was observed by the CS (2–1) emission (Ciardi et al. 2000). To calculate $|\vec{B}_{\rm pos}|$, they used Eq. (4) in Crutcher (2004) of $|\vec{B}_{\rm pos}| \approx 9.3\sqrt{n({\rm H_2})}\ \frac{\Delta v_{\rm FWHM}}{\delta\phi}\ \mu$G where $\delta\phi$ is the dispersion in a polarization angle in degrees. Since we have the revised mean velocity width of $\Delta v_{\rm FWHM} = 0.69 \pm 0.12$ km s^{-1} (§4.3) and the number density of $n_c({\rm H_2}) = 800 \sim 4200$ cm^{-3} (§5.2), we recalculated $|\vec{B}_{\rm pos}|$ of $55 \pm 30\ \mu$G. Here we assumed that the $\delta\phi$ value of 5.9° derived from the infrared data towards the CS (2–1) core (Poidevin & Bastien 2006) holds in the region we observed.

With the magnetic field strength, we estimate the magnetic pressure of $\log P_{\rm mag} = \log\left(B^2/8\pi\right) = -10.6 \sim -9.5$ which is larger than the effective internal pressure of the filament given by $\log P_{\rm eff} \equiv \log\left\{\rho\left(c_s^2 + \sigma^2_{\rm nth}\right)\right\} = -11.3 \sim -10.6$. Considering the

Table 1
Physical Properties of the Filament Gas Around the GF 9-2 Core

Property	Value	Unit	Section
$T_{\rm gas}$[a]	7.5±1.0	K	§4.2
$\langle N_{\rm H_2}\rangle$[b]	(2.7±0.9)×10^{21}	$\rm cm^{-2}$	§4.4
$\langle\sigma_{\rm nth}/c_{\rm s}\rangle$[c]	2.1±0.5	...	§5.1
$M_{\rm LTE}/M_{\rm crit}^{\rm eff}$	0.5±0.2	...	§5.3.1
H[d]	0.3 ∼ 0.7	pc	§5.3.1
$n_{\rm c}(\rm H_2)$[e]	800 ∼ 4200	$\rm cm^{-3}$	§5.2
$\lvert\vec{B}_{\rm pos}\rvert$[f]	55 ± 30	μG	§5.4
$P_{\rm eff}/P_{\rm mag}$	0.03 ∼ 0.2	...	§5.4

[a] Gas temperature
[b] Mean column density of $\rm H_2$ molecules
[c] Mean Mach number defined by the ratio of non-thermal velocity dispersion ($\sigma_{\rm nth}$) to the sound velocity ($c_{\rm s}$)
[d] Scale height
[e] Central volume density of $\rm H_2$ molecules
[f] Magnetic field strength in the plane of the sky

ratio of $P_{\rm eff}/P_{\rm mag}$ =0.03∼0.2 (Table 1), we speculate that the significant magnetic pressure can support the filament against the axial fragmentation.

Subsequently, we examine whether or not the large scale magnetic field can support the GF 9-2 core through a comparison of,

$$\frac{\left|\frac{M}{\Phi}\right|_{\rm GF\,9-2}}{\left|\frac{M}{\Phi}\right|_{\rm critical}} = \frac{\frac{M_{\rm LTE}}{|\vec{B}_{\rm pos}|\,R_{\rm eff}^2}}{\frac{M_0}{B_0 R_0^2}} = \frac{\frac{(1.3\pm0.5)\,M_\odot}{(\mathbf{55}\pm\mathbf{30})\mu{\rm G}\cdot(0.032\,{\rm pc})^2}}{\left(\frac{5}{9G}\right)^{1/2}} \sim \frac{(4.8^{+9.9}_{-2.9})\times10^3}{2900} \sim 2^{+3}_{-1} \quad (8)$$

where the denominator is the critical mass-to-magnetic-flux ratio for a uniform spherical cloud, and the numerator is the ratio for the GF 9-2 dense core traced by the $\rm H^{13}CO^+$ and $\rm N_2H^+$ lines (the $M_{\rm LTE}$ and $R_{\rm eff}$ values are taken from Table 8 in paper I), which exists in the large-scale magnetic field (Figure 16). Although the non-dimensional coefficient in the relation of $\left|\frac{M}{\Phi}\right|_{\rm cr} \propto \frac{1}{\sqrt{G}}$ differs in various models (see e.g., Lang 1980; Shu 1992; Lequeux 2005; Bodenheimer 2011, and references therein), such a difference is negligible compared to the uncertainty in the estimate of the magnetic field strength (§5.4) and that in the $M_{\rm LTE}$ estimate due to the uncertain fractional abundances of the tracers. The above comparison suggests that the GF 9-2 core is in magnetically super critical state, which does not contradict the fact that the core is dynamically collapsing because no magnetic fields can halt such collapse once it has begun.

5.5. *Core Formation in the Filament*

The discussion so far indicates that the natal gas of the GF 9-2 core is supported by the turbulent and magnetic pressures against its self-gravity. In Table 1, we summarize the derived physical properties of the natal filamentary gas. Recall that the central 30″ region of the dense core, corresponding to a diameter of ∼0.06 pc at d = 200 pc, is dynamically infalling onto the protostar (papers I and III). These facts reinforce our assertion that a dynamically collapsing core formed in a gravitationally stable filament. Such a scenario immediately raises the following questions: how have the turbulence and the magnetic fields decayed locally at the spatial scale of the core?; can such dissipation determine the initial conditions of the core collapse? The answer to the former may be that such a spatial scale was set by the Jeans length of the tenuous gas. As for the latter, we require that the dissipation time scales of the supersonic turbulence ($t_{\rm turb}^{\rm disp}$) and the magnetic fields ($t_{\rm mag}^{\rm disp}$) are less than the free-fall time ($t_{\rm ff}$) of the gas traced by the ^{13}CO line. After addressing these issues, we discuss the nature of the south-western condensation.

5.5.1. *The GF 9-2 Core: An Unstable Core in the Stable Filament*

Theoretical studies have predicted the presence of gravitationally unstable cores in a stable filament. For instance, 3D simulations by Klessen et al. (2000, 2005) showed that density enhancements caused by strong shocks can produce gravitationally unstable dense cores, despite the fact that parental clouds are being prevented from the global collapse because of the turbulent support. In other words, a local collapse can occur even in the turbulent-supported self-gravitating global medium (Klessen et al. 2000). Although their calculations did not include the effect of magnetic fields, their results are reconciled with the previous low-resolution 2D calculations considering magnetic fields(Vázquez-Semadeni et al. 1996). Subsequent numerical simulations (e.g., Mac Low 1999; Ostriker et al. 2001; Vázquez-Semadeni et al. 2005; Heitsch et al. 2009) with magnetic fields claim that the core formation must have completed within the global free-fall time of the natal cloud gas. A recent theoretical study by Leão et al. (2013) demonstrated that magnetic flux can be quickly removed from a cloud core by magnetic reconnection diffusion, which removes the magnetic flux through reconnection of the field lines by the co-existing turbulence (not by ambipolar diffusion) with a time scale as short as $t_{\rm ff}$.

Contrary to these theoretical predictions, we propose a simple scenario that the supersonic turbulence and the magnetic fields locally decayed at the spatial scale comparable to the Jeans length of the filament gas: $\lambda_{\rm J}$ = 0.3 ∼ 0.6 pc for $T_{\rm kin}$= 7.5 K and $n_{\rm H_2}$ = 800 ∼ 4200 $\rm cm^{-3}$ (§5.3.1). Once the dissipation of the turbulence and the magnetic fields had occurred locally over a region with size scale of the Jeans length, the region lost the support against self-gravity and contracted into a compact gas clump with 0.1 pc size, i.e., a typical size of a low-mass star forming cloud core, by increasing its density as high as $\sim 10^3$ $\rm cm^{-3}\times(\lambda_J/0.1\,pc)^3$ = (3 ∼ 22) × 10^4 $\rm cm^{-3}$. With this number density, the $\rm NH_3$ (1,1) lines (critical density of $n_{\rm crit}$ ∼ 10^4 $\rm cm^{-3}$) and the $\rm H^{13}CO^+$ (1–0) and $\rm N_2H^+$ (1–0) transitions ($n_{\rm crit}$ ∼ 10^5 $\rm cm^{-3}$) can be collisionally excited. Because the latter higher density tracers were detected towards the GF 9-2 core, the above argument may favor the larger side of $\lambda_{\rm J}$ ∼ 0.6 pc. An alternative idea is that the core formed as a result of internal shock in the filament. However, this is unlikely because the shock compression with a Mach number ($\mathcal{M}$) of ∼ 2 (§5.1) would increase the gas density by a factor of $\mathcal{M}^2$ in the case of the J-type shock (Spitzer 1978),

i.e., up to at most $\sim 10^3$ cm^{-3} $\times 2^2 < 10^4$ cm^{-3}. Clearly this is lower than the critical densities of the N_2H^+ and $H^{13}CO^+$ lines.

Next, we examine whether the relation of $t_{\rm turb}^{\rm disp} \lesssim t_{\rm ff}$ holds or not. Assuming that the core formed through the local dissipation of the supersonic turbulence with a spatial scale of $\lambda_{\rm J} = 0.3 \sim 0.6$ pc, the dissipation time scale is given by,

$$t_{\rm turb}^{\rm disp} \sim \frac{\lambda_{\rm J}}{\sigma_{\rm nth}} \sim 10^6 \left(\frac{\lambda_{\rm J}}{0.3 \sim 0.6\,{\rm pc}}\right) \left(\frac{\sigma_{\rm nth}}{0.34\,{\rm km\,s^{-1}}}\right)^{-1} {\rm yrs}, \quad (9)$$

for the natal Component 1 gas. The other time scale to assess the core formation process is the free-fall time of,

$$t_{\rm ff} = \sqrt{\frac{3\pi}{32 G \rho}} \sim 10^6 \left(\frac{n_{\rm H_2}}{800 \sim 4200\,{\rm cm^{-3}}}\right)^{-1/2} {\rm yrs}. \quad (10)$$

The two time scales are comparable to each other within large uncertainties, hence we conclude that $t_{\rm turb}^{\rm disp} \sim t_{\rm ff}$ holds.

Last, we attempt to give some constraints on the dissipation time scale of the magnetic fields ($t_{\rm mag}^{\rm disp}$). The upper limit of $t_{\rm mag}^{\rm disp}$ may be estimated by the ambipolar diffusion time scale ($t_{\rm AD}$) for a spherical cloud with a radius of $R \sim \lambda_{\rm J}/2$ assuming a typical ionization degree in the ISM [see e.g., Eq.(10.5) in Stahler & Palla (2005) and Eq.(2.51) in Bodenheimer (2011)] as,

$$t_{\rm mag}^{\rm disp} \lesssim t_{\rm AD} \sim 10^5 - 10^8 \left(\frac{n_{\rm H_2}}{800 \sim 4200\,{\rm cm^{-3}}}\right)^{\frac{3}{2}} \times \left(\frac{B}{55 \pm 30\,\mu{\rm G}}\right)^{-2} \left(\frac{R}{0.2 \sim 0.3\,{\rm pc}}\right)^{2} {\rm yrs}. \quad (11)$$

The lower limit of $t_{\rm mag}^{\rm disp}$ might be given by the time scale of the magnetic reconnection diffusion ($t_{\rm MRD}$) which should be comparable to or less than $t_{\rm ff}$ (Leão et al. 2013). Hence we may have a very robust constraint of $t_{\rm ff} \lesssim t_{\rm mag}^{\rm disp} \lesssim 100\,t_{\rm ff}$. We, however, speculate that $t_{\rm mag}^{\rm disp} \sim 100\,t_{\rm ff}$ is very unlikely because the Eq.(11) assumes a constant density and a uniform magnetic field for a quiescent cloud.

We therefore discuss that the formation of the GF 9-2 core was triggered by the local dissipation(s) of the supersonic turbulence and probably the magnetic fields with the time scale comparable to $t_{\rm ff}$, i.e., the "fast mode" of star formation (§1). Namely this scenario naturally produces an unstable core collapsing in a runaway fashion.

5.5.2. *The South-Western Condensation with Velocity Width Enhancement: A "Protocore" Prior To a Dense Core?*

We discuss the nature of another well-defined object discovered by our observations, i.e., the south-western condensation where both the temperature and velocity width of the gas are enhanced. Neither indirect evidence for star formation, such as the presence of a point-like infrared source, masers, radio continuum emission, and a molecular outflow nor dense gas emission, such as NH_3(1,1) lines, has been reported towards the region (Ciardi et al. 1998, 2000; Poidevin & Bastien 2006, paper II). Hence, the $C^{18}O$ (1–0) emission shown in Figure 2c is the densest gas tracer detected towards the region.

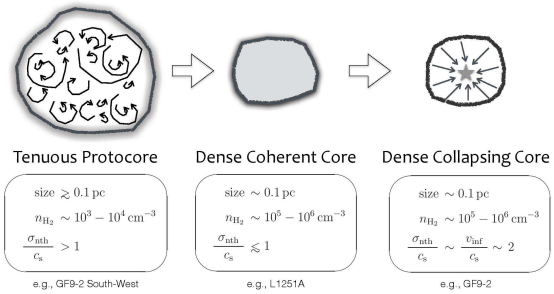
Tenuous Protocore
Dense Coherent Core
Dense Collapsing Core
size $\gtrsim 0.1$ pc
$n_{\rm H_2} \sim 10^3 - 10^4$ cm^{-3}
$\frac{\sigma_{\rm nth}}{c_{\rm s}} > 1$
size ~ 0.1 pc
$n_{\rm H_2} \sim 10^5 - 10^6$ cm^{-3}
$\frac{\sigma_{\rm nth}}{c_{\rm s}} \lesssim 1$
size ~ 0.1 pc
$n_{\rm H_2} \sim 10^5 - 10^6$ cm^{-3}
$\frac{\sigma_{\rm nth}}{c_{\rm s}} \sim \frac{v_{\rm inf}}{c_{\rm s}} \sim 2$
e.g., GF9-2 South-West
e.g., L1251A
e.g., GF9-2

Figure 17. Schematic illustration of the proposed scenario for the evolution of a low-mass star-forming cloud core in the "fast mode" of star formation, i.e., the runaway collapse scenario (Larson 1969; Penston 1969; Hunter 1977). The dense core of L1251 A is proposed to be a "coherent core" which has $\langle \sigma_{\rm nth}/c_{\rm s} \rangle \lesssim 1$ (Goodman et al. 1998; Barranco & Goodman 1998). Here $\sigma_{\rm nth}$ denotes non-thermal velocity dispersion, $c_{\rm s}$ isothermal sound velocity, and $v_{\rm inf}$ infall velocity of the gas. See §1 and §5.5.2 for details.

As mentioned above, we reject the possibility that the condensation represents a molecular outflow lobe driven by the protostar embedded in the GF 9-2 core for the following reasons. First, we did not detect any high velocity wing emission in the ^{12}CO spectrum towards the condensation (see Figure 5b), which is evidence for a well-developed outflow. Second, our recent interferometric observations of the ^{12}CO (3–2) line with the SMA clearly demonstrated the presence of a compact ($\sim 5 \times 10^{-3}$ pc) molecular outflow driven by the 3 mm continuum source in the GF 9-2 core (Furuya et al. 2014, Furuya et al. in prep.). Therefore we argue that the south-western condensation may be a precursor of a dense cloud core, i.e., *protocore*.

In order to verify such an interpretation, we need to assess the dynamical state of the condensation, hence we estimated the spatial extent of the condensation using the results from Figures 11 and 12. With the 90% percentile of $N_{\rm H_2} = 3.9 \times 10^{21}$ cm^{-2} in Figure 12 a closed contour is uniquely defined for the condensation. In Figure 11, the 70% percentile of $N_{\rm H_2} = 3.6 \times 10^{21}$ cm^{-2} encloses both the GF 9-2 core and the condensation by a single contour. We therefore judged that these contours should give us a robust size range which is presented by an effective radius of $r_{\rm eff} = 0.09 \sim 0.14$ pc. Here we used $r_{\rm eff} = \sqrt{A/\pi}$ where A is the area enclosed by the contour. We obtained a column density range of $(3.6 \sim 3.9) \times 10^{21}$ cm^{-2}, leading to an $M_{\rm LTE}$ range of $1.9 \sim 4.3\,M_\odot$ with the fixed X(^{13}CO) value. We also estimated that $\Delta v_{\rm FWHM}$ ranges $1.1 \sim 1.2$ km s^{-1} from Figure 10c (corresponding to the velocity dispersion range of $0.47 \sim 0.50$ km s^{-1}), yielding $\langle \sigma_{\rm nth}/c_{\rm s} \rangle \sim 3$. These quantities lead to an energy balance based on the Virial theorem between the supersonic turbulence and the self-gravity for a uniform spherical cloud of,

$$\frac{E_{\rm turb}}{|E_{\rm grav}|} = \frac{\frac{3}{2} M_{\rm LTE} \sigma^2}{\left| -\frac{3}{5} \frac{G M_{\rm LTE}^2}{r_{\rm eff}} \right|} = 1 \sim 13, \quad (12)$$

suggesting that the condensation may be dispersed by the turbulence. It should be noted that, if we include the uncertainty in the $X(^{13}{\rm CO})$ (a factor of 3) for the $M_{\rm LTE}$ estimate (§4.4), the possibility that the condensation is gravitationaly bound is not completely ruled out. On

the other hand, the south-western condensation seems in magnetically subcritical state because of,

$$\frac{\left|\frac{M}{\Phi}\right|_{\rm protocore}}{\left|\frac{M}{\Phi}\right|_{\rm critical}} = \frac{400 \sim 5000}{2900} = 0.1 \sim 2, \qquad (13)$$

using Eq.(8) for the above $M_{\rm LTE}$ and $r_{\rm eff}$ ranges.

If the south-western condensation is not gravitationally bound, it must be a transient object which will eventually disperse by the turbulence with the time scale of $2r_{\rm eff}/\sigma \sim 10^5$ yrs. We speculate that it might be a "failed core" in Vázquez-Semadeni et al. (2005), a biproduct from core formation. Alternatively, if the magnetic pressure overcomes the turbulent one, the magnetic fields should sustain the condensation.

If the condensation is gravitationally bound, it may be a precursor of a low-mass star-forming dense core, *protocore*, which is at an evolutionary phase before the dissipation of the supersonic turbulence (see Figure 17). More specifically, we consider that the evolutionary phase of this object is prior to the coherent core phase, which is characterized by $\langle\sigma_{\rm nth}/c_{\rm s}\rangle \lesssim 1$ (Goodman et al. 1998; Barranco & Goodman 1998; Caselli et al. 2002; Pineda et al. 2010). Such a *protocore* interpretation is consistent with the following two facts. First, the object is two times larger than that of a typical low-mass star-forming core. If the object contracts to half its size, its mean density would increase up to $\sim 10^4$ cm^{-3} which can be traced by e.g., collisionally excited NH_3 (1,1) emission. Second, the object is massive ($\sim 5M_\odot$) enough to evolve towards a typical cloud core, regardless of an $\eta_{\rm CF}$ value (§5.3.2). Since the GF 9 filament is likely gravitationally stable (§5.2 and §5.3), we argue that the formation of the *protocore* was triggered by a collision between the Components 1 and 2. In this scenario, the velocity width enhancement is interpreted as the sum of the turbulent motions in the two components and the radial velocity difference between them. The difference is estimated to be $\Delta v_{\rm diff} \sim 1$ km s^{-1} from Figures 5b and 10b, suggestive of a weak collision with $\mathcal{M} \sim 2-3$. It is a non-trivial issue to estimate analytically how much the gas temperature is raised (§4.2) due to the weak collision (it is possibly a C-type shock). Nevertheless, we believe that the cloud-cloud collision scenario reasonably explains the observed enhancements of the gas temperature and velocity width. Similar to the case of the GF 9-2 core (§5.5.1), an unstable core is anticipated to form under the conditions with a collision time scale of $t_{\rm coll} \sim 2r_{\rm eff}/\Delta v_{\rm diff} \sim 10^5$ yrs, which is comparable to $t_{\rm ff}(\sim t_{\rm turb}^{\rm disp} \sim t_{\rm mag}^{\rm disp})$ of 10^5 yrs for the condensation gas.

6. SUMMARY

Analyzing the CO isotopologue data taken with the Nobeyama 45 m telescope, we have studied the physical properties of the low density ($\sim 10^3$ cm^{-3}) filament gas surrounding the GF 9-2 dense cloud core which harbors the exceptionally young protostar. Our main results are summarized as follows.

1. The ^{13}CO map covering a $\sim 0.78 \times 0.78$ pc^2 square field centered on the core clearly shows the filamentary morphology. The C^{18}O map demonstrates that the GF 9-2 core formed at the local intensity maxima of the filament. Solving the optical depths and excitation temperatures of the CO isotopologue lines, we made the opacity-free ^{13}CO spectra which were used to produce spectral momentum maps.

2. On the basis of the spatial and velocity structures of the filament gas, we identified two gas components, one of which is the natal filament of the GF 9-2 dense core (Component 1). The centroid velocity map shows that the Component 1 is confined in a rather narrow LSR-velocity range of ~ 0.6 km s^{-1}, and does not show any systematic motions. In contrast, the velocity width is enhanced up to $\Delta v_{\rm FWHM} = 1.4$ km s^{-1} to the south-west of the core. A mean velocity dispersion of the south-western region is $\sigma = 0.47$ km s^{-1}.

3. Using the optical depth, excitation temperature, and velocity width maps, we calculated the H_2 column density. The column density map clearly traces the natal filament of the GF 9-2 core, and the core is located at the local column density peak in the filament. Furthermore, the column density histogram is well described by a log-normal function, suggesting that the supersonic turbulence governs the density structure of the filament.

4. The mean temperature of the gas in the observed area is 7.5 K with a standard deviation of 1.0 K. Subtracting the contributions of thermal gas motions from the $\Delta v_{\rm FWHM}$ map, we made a ratio map between the non-thermal velocity dispersion and the local sound speed ($\sigma_{\rm nth}/c_{\rm s}$). The map clearly demonstrates that the natal tenuous filament is in a supersonic turbulent state whose Mach number ranges from 0.96 to 3.4 with a mean of 2.1.

5. Considering the turbulent pressure into a model of an isothermal cylinder in hydrostatic equilibrium, we assessed the dynamical stability of the filament. The maximum mass that can be radially supported by the internal pressures (predominantly the turbulent pressure) is estimated to be $M_{\rm crit}^{\rm eff} = 51^{+32}_{-22}\ M_\odot$. On the other hand, we obtained the LTE mass of $24\pm10\ M_\odot$, suggestive of a gravitationally stable state against radial collapse. Furthermore, analyzing the column density map on the basis of the isothermal cylinder model, we estimated a scale height of the filament to be $H = 0.3 \sim 0.7$ pc, yielding the central number density of $n_{\rm c}(H_2) = 800 \sim 4200$ cm^{-3}. Since the NH_3 core masses in the filament are smaller than those expected in the axial unstable modes, the filament is likely to be gravitationally stable against axial fragmentation as well.

6. With the $\langle\sigma_{\rm nth}\rangle$ of 0.34 ± 0.80 km s^{-1} and the $n_{\rm c}(H_2) = 800 \sim 4200$ cm^{-3}, we recalculated the strength of the large-scale well-aligned magnetic fields in the natal filament gas to be $|B| = 55\pm30\ \mu$G by following the Chandrasekhar & Fermi method in Poidevin & Bastien (2006).

7. The transverse magnetic field can support the filament against the axial collapse, because the magnetic pressure appears to exceed the internal (thermal and turbulent) gas pressure. In contrast, the GF 9-2 core is in a magnetically super critical state through a comparison of the mass-to-magnetic-flux ratio of the core with the theoretical critical value. This inference agrees with the previous results that the core is dynamically collapsing.

8. The dissipation time of the supersonic turbulence is comparable to the free-fall time of the natal tenuous gas of 10^6 yrs within the uncertainties. Although the dissipation time of the magnetic fields has large uncertainties, we consider that the local dissipation(s) of the turbulence and the magnetic fields made a part of the filament gas unstable, resulting in the formation of the gravitationally unstable GF 9-2 core.

9. The south-western condensation, where the gas temperature and velocity width are enhanced, may be a precursor of a low-mass star forming cloud core, *protocore*, if it is gravitationally bound. The formation of the south-western *protocore* must have been triggered by a collision between the two gas components. Because of $\langle \sigma_{\rm nth}/c_{\rm s} \rangle \sim 3$, the evolutionary stage of the south-western *protocore* is highly likely before the phase of the coherent dense core which is characterized by $\langle \sigma_{\rm nth}/c_{\rm s} \rangle \lesssim 1$ (Goodman et al. 1998).

We sincerely acknowledge the anonymous referee whose comments significantly helped to improve our data presentation and the quality of the discussion. R. S. F. gratefully acknowledges T. Sawada, S. Takahashi, A. Higuchi, and N. Kuno for their generous help during the observations, K. Schubert and J. Noumaru for their help in computing, and P. T. P. Ho, N. Hirano, M. Taffalla, A. Hacar, J. M. Torrelles, R. Cesaroni, K. Tomisaka, M. N. Machida, T. Inoue, S. Inutsuka, and Y. Fukui for fruitful discussion. R. S. F. also acknowledges R. Kawabe, M. Hayashi, H. Takami, N. Arimoto, T. Usuda, H. Araki, and Y. Takaishi for their continuous support and encouragement. The authors sincerely thank Daniele Galli for a critical reading of the manuscript at the last stage of preparation. This work was partially supported by Grant-in-Aids from the Ministry of Education, Culture, Sports, Science and Technology of Japan (No. 20740113), International Exchange Support Program of Foundation for Promotion of Astronomy (Tenmon Zaidan) of Japan, the JSPS Institutional Program for Young Researcher Overseas Visits (Wakate Haken), the NAOJ grants for domestic universities and institutes (Daigaku Shien), and AWA Support Center at the University of Tokushima.

Facilities: Nobeyama 45 m telescope

APPENDIX

OPTICAL DEPTH AND EXCITATION TEMPERATURE OF THE ^{13}CO $J = 1 - 0$ LINE EMISSION

Radiative Transfer Equation

The main beam brightness temperature ($T_{\rm mb}$) of molecular line emission emanated from a homogeneous gas cloud is written by,

$$T_{\rm mb}(v) = f\{J_\nu(T_{\rm ex}) - J_\nu(T_{\rm bg})\}[1 - \exp\{-\tau(v)\}], \tag{A1}$$

where $\tau(v)$ is the optical depth of the line as a function of radial velocity, v, f is the beam filling factor, $T_{\rm ex}$ the excitation temperature of the line, and $T_{\rm bg}$ the temperature of the cosmic background radiation. The function $J_\nu(T)$ is the radiation temperature defined by $\frac{h\nu}{k}\frac{1}{\exp(h\nu/kT)-1}$ where ν is the frequency of the line, T the gas temperature, k the Boltzmann constant, and h the Planck constant.

Estimate of Optical Depth and Excitation Temperature

The optical depth and excitation temperature of the ^{13}CO (1–0) line can be estimated by applying Eq.(A1) to a set of CO isotopologue spectra, assuming the abundance ratios between ^{12}CO and ^{13}CO, and between ^{13}CO and C^{18}O. For simplicity, we assumed that the ^{12}CO (1–0) line at rest frequency of 115.271202 GHz, the ^{13}CO (1–0) line at 110.201353 GHz, and the C^{18}O (1–0) line at 109.782173 GHz are excited with a common $T_{\rm ex}$ at each spatial position; we also assumed $J_{115\,\rm GHz}(T) = J_{110\,\rm GHz}(T)$ and $f = 1.0$. Adopting the solar abundance ratios of $\alpha \equiv [^{12}{\rm CO}]/[^{13}{\rm CO}] = 89$ and $\beta \equiv [^{13}{\rm CO}]/[{\rm C}^{18}{\rm O}] = 5.5$ (e.g., Lang 1980; Garden et al. 1991; Lequeux 2005), we solved the following equations for τ and a quantity of A defined by $J_{110\,\rm GHz}(T_{\rm ex}) - J_{110\,\rm GHz}(T_{\rm bg})$ at each pixel in the 3-dimensional (3D) space of right ascension offset ($\Delta\alpha$), declination offset ($\Delta\delta$), and LSR-velocity ($V_{\rm LSR}$);

$$\begin{aligned} T_{12} &= A(1 - e^{-\alpha\tau}), \\ T_{13} &= A(1 - e^{-\tau}), \\ T_{18} &= A(1 - e^{-\tau/\beta}), \end{aligned} \tag{A2}$$

where T_{12}, T_{13}, and T_{18} are the main beam brightness temperatures of the ^{12}CO, ^{13}CO, and C^{18}O isotopologue lines, respectively.

In the following, we describe our analysis by showing the CO spectra observed towards the GF 9-2 core center as an example (Figure 18a). We started the analysis by calculating the line intensity ratios of $R_{12/13} = T_{12}/T_{13}$ and

$R_{13/18} = T_{13}/T_{18}$ at each velocity channel (Figure 18b). On the basis of these ratios, we divided all the velocity channels into the following four cases,

$$\begin{aligned}
&\text{case (i)}: \ 1.0 < R_{12/13} < \alpha \text{ and } T_{18} < 3\Delta T^{18}_{\rm rms},\\
&\text{case (ii)}: \ 1.0 < R_{13/18} < \beta \text{ and } (R_{12/13} > \alpha \text{ or } T_{12} < 3\Delta T^{12}_{\rm rms}),\\
&\text{case (iii)}: \ 1.0 < R_{12/13} < \alpha \text{ and } 1.0 < R_{13/18} < \beta,
\end{aligned} \tag{A3}$$

and

$$\text{case (iv)}: \ (0.0 < R_{12/13} < 1.0 \text{ or } R_{12/13} \geq \alpha) \text{ and } (0.0 < R_{13/18} < 1.0 \text{ or } R_{13/18} \geq \beta),$$

where $\Delta T^{12}_{\rm rms}$ and $\Delta T^{18}_{\rm rms}$ denote the RMS noise levels in $T_{\rm mb}$ for the ^{12}CO, and C^{18}O lines, respectively. As seen in the above, we adopted detection threshold of 3σ. We did not consider the case that only the ^{12}CO line is detected, as we cannot define an intensity ratio.

Case (i) is the category where both the ^{12}CO and ^{13}CO lines are detected with $T_{12} > T_{13}$, but the C^{18}O line does not show significant emission. Case (ii) corresponds to the category that both the ^{13}CO and C^{18}O lines are detected with $T_{13} > T_{18}$, but the ^{12}CO line is too strong or is not detected. Case (ii) is often found near the velocity channels where the ^{12}CO line suffers self-absorption and the ^{13}CO one shows intense emission (see Figure 18a). For Cases (i) and (ii), we numerically solved the following equations for τ:

$$\begin{aligned}
R_{12/13} &= \tfrac{1-e^{-\alpha\tau}}{1-e^{-\tau}} \quad \text{for case (i)},\\
R_{13/18} &= \tfrac{1-e^{-\tau}}{1-e^{-\tau/\beta}} \quad \text{for case (ii)}.
\end{aligned} \tag{A4}$$

We employed the bisection method with an accuracy of 0.001, and performed about 10 repetitions for many cases, as expected from $1/2^{10} \sim 0.001$. After obtaining τ, we calculated $T_{\rm ex}$ using Eq.(A2). In the 3D space of ($\Delta\alpha$, $\Delta\delta$, $V_{\rm LSR}$) where we have a total of $72 \times 72 \times 150 = 7.775 \times 10^5$ points, we obtained solutions at 34668 points for Case (i) and 784 points for Case (ii), which correspond to 4155 and 632 spatial positions in the ($\Delta\alpha$, $\Delta\delta$) coordinates, respectively.

Case (iii) is a category where all three lines are detected with an intensity order of $T_{12} > T_{13} > T_{18}$, allowing us to utilize the maximum likelihood method on the basis of χ^2. We searched the best-fit values for τ and A by minimizing the χ^2 value defined by

$$\chi^2 = \sum_{i=12,\,13,\,18} \left(\frac{T_i - T_i^{\rm model}}{\Delta T^i_{\rm rms}} \right)^2, \tag{A5}$$

where $T_{12}^{\rm model} = A(1-e^{-\alpha\tau})$, $T_{13}^{\rm model} = A(1-e^{-\tau})$, and $T_{18}^{\rm model} = A(1-e^{-\tau/\beta})$. In order to give better initial guesses for the likelihood method analysis, we solved Eq.(A4) for τ and A by means of the bisection method before performing χ^2-fitting. We calculated the ^{13}CO optical depths from both the $R_{12/13}$ and $R_{13/18}$, and adopted the mean value between them as the center of the "searching area" in the A-τ plane (see Figure 19) for finding the minimum χ^2 value, $\chi^2_{\rm min}$. In the ($\Delta\alpha$, $\Delta\delta$, $V_{\rm LSR}$) space, there are 449 points that satisfy the criteria for Case (iii), corresponding to 328 positions in the ($\Delta\alpha$, $\Delta\delta$) space. For the 449 points we calculated that the $\chi^2_{\rm min}$ values have a minimum of 0.10, a maximum of 8.0, a mean of 0.69, a standard deviation of 1.0, and a median of 0.29. Since the obtained $\chi^2_{\rm min}$ is distributed around unity, our estimates of τ and A are considered to be reasonable.

Case (iv) corresponds to the data sets where either the ^{12}CO or/and ^{13}CO line shows self-absorption or their intensity ratios are inconsistent with those expected from the given abundance ratios. We identified 20 points in the 3D space for such a case, which may be negligible compared to the numbers of the solutions obtained in the above three cases because it corresponds to 1.7% of all the analyzed data points. Eleven out of the twenty points are found either at the boundary LSR-velocity between the Components 1 and 2, $V_{\rm LSR} = -2.2$ km s^{-1} defined in §3, or at the adjacent channels. Since such anomaly ratios do not allow us to estimate τ and $T_{\rm ex}$, we estimated τ from the observed T_{13} value using an empirical relation between τ and T_{13} obtained from the Case (iii) analysis; $T_{13} = (3.95 \pm 0.02)[1 - \exp\{-(1.68 \pm 0.03)\tau\}]$ for $\tau \geq 0.1$. After obtaining τ by this way, we calculated $T_{\rm ex}$ using Eq.(A2).

In summary, we obtained a set of (τ, $T_{\rm ex}$) values at a total of 36622 points in the ($\Delta\alpha$, $\Delta\delta$, $V_{\rm LSR}$) space; these are 34668 points from Case (i), 784 points from Case (ii), 1154 points from Case (iiI), and 20 points from Case (iv).

Error Estimates for the Optical Depth and Excitation Temperature

In this subsection, we describe error estimates for the optical depth and excitation temperature of the ^{13}CO emission. Figures 20 and 21 show observed velocity channel maps of the uncertainties in the ^{13}CO optical depth and excitation temperature, respectively. Comparing Figures 7 with 20 and Figures 8 with 21, we found that the resultant uncertainties in the τ and $T_{\rm ex}$ are 15% with respect to their values.

Error Estimates for Cases (i) and (ii)

Since the ^{13}CO optical depth in Eq.(A4) cannot be explicitly solved, we estimated the uncertainty in τ of $\Delta\tau_{\rm rms}$, as follows. In the Case (ii), for example, the ratio $R_{13/18}$ is considered to be a function of τ, and thus the following

equation holds,

$$(\Delta R_{13/18}^{\rm rms})^2 = \left(\frac{\partial R_{13/18}}{\partial \tau}\right)^2 (\Delta\tau_{\rm rms})^2. \tag{A6}$$

Furthermore, recall that the ratio $R_{13/18}$ is defined by $R_{13/18} = T_{13}/T_{18}$ where the two temperatures of T_{13} and T_{18} have the uncertainties of $\Delta T_{13}^{\rm rms}$ and $\Delta T_{\rm rms}^{18}$, respectively. Therefore, we have,

$$(\Delta R_{13/18}^{\rm rms})^2 = \left(\frac{\partial R_{13/18}}{\partial\ T_{13}}\right)^2 (\Delta T_{13}^{\rm rms})^2 + \left(\frac{\partial R_{13/18}}{\partial\ T_{18}}\right)^2 (\Delta T_{18}^{\rm rms})^2\,. \tag{A7}$$

Here the covariance, $\langle \Delta T_{13}^{\rm rms} \cdot \Delta T_{18}^{\rm rms}\rangle$, was set to be zero because the two variables are independent of each other. Combining Eqs.(A6) and (A7), we can write the desired $\Delta\tau_{\rm rms}$ by

$$(\Delta\tau_{\rm rms})^2 = \left(\frac{\partial R_{13/18}}{\partial \tau}\right)^{-2} \left\{ \left(\frac{\partial R_{13/18}}{\partial\ T_{13}}\right)^2 (\Delta T_{13}^{\rm rms})^2 + \left(\frac{\partial R_{13/18}}{\partial\ T_{18}}\right)^2 (\Delta T_{18}^{\rm rms})^2 \right\} \tag{A8}$$

where $\frac{\partial}{\partial\tau} R_{13/18} = \frac{e^{-\tau}}{1-\exp(-\tau/\beta)} - \frac{e^{-\tau/\beta}(1-e^{-\tau})}{\beta\{1-\exp(-\tau/\beta)\}^2}$, $\frac{\partial}{\partial\ T_{13}} R_{13/18} = \frac{1}{T_{18}}$ and $\frac{\partial}{\partial\ T_{18}} R_{13/18} = -\frac{T_{13}}{T_{18}^2}$. After obtaining $\Delta\tau_{\rm rms}$, we subsequently calculated the uncertainty in $T_{\rm ex}$ of $\Delta T_{\rm rms}^{\rm ex}$ through the relationship from Eq.(A2) as follows,

$$\left(T_{13} - T_{13}^{\rm model}\right)^2 = \left(\frac{\partial\ T_{13}}{\partial\tau}\right)^2 (\Delta\tau_{\rm rms})^2 + \left(\frac{\partial\ T_{13}}{\partial T_{\rm ex}}\right)^2 (\Delta T_{\rm ex}^{\rm rms})^2 \tag{A9}$$

where $\frac{\partial T_{13}}{\partial\tau} = Ae^{-\tau}$ and $\frac{\partial T_{13}}{\partial T_{\rm ex}} = \left(\frac{h\nu}{kT_{\rm ex}}\right)^2 \frac{\exp(h\nu/kT_{\rm ex})\{1-\exp(-\tau)\}}{\{\exp(h\nu/kT_{\rm ex})-1\}^2}$. Replacing $\Delta\tau_{\rm rms}$ with Eq.(A8), the desired $\Delta T_{\rm ex}^{\rm rms}$ can be explicitly written as a function of T_{13}, T_{18}, $\Delta T_{13}^{\rm rms}$, $\Delta T_{18}^{\rm rms}$, $T_{\rm ex}$, and τ.

Error Estimates for Case (iii)

For the Case (iii) where we performed the maximum likelihood analysis, the uncertainties of the best-fit parameters, i.e., the 68.3% confidence intervals for the two "parameters of interest", are given by the projections onto the τ- and A-axes of the "confidence region ellipse" where the function $\chi^2(\tau, A)$ takes a value of $\chi^2_{\rm min} + 2.30$ (Press et al. 2010, p.815). Figure 19 presents an example showing such an error analysis at the $V_{\rm LSR} = -2.6$ km s^{-1} channel of the spectra shown in Figure 18a. After numerically obtaining $\Delta A_{\rm rms}$, we calculated $\Delta T_{\rm ex}^{\rm rms}$ through $(\Delta A_{\rm rms})^2 = \left(\frac{\partial A}{\partial T_{\rm ex}}\right)^2 (\Delta T_{\rm ex}^{\rm rms})^2$ where $\frac{\partial A}{\partial T_{\rm ex}} = \left(\frac{h\nu}{kT_{\rm ex}}\right)^2 \frac{\exp(h\nu/kT_{\rm ex})\{1-\exp(-\tau)\}}{\{\exp(h\nu/kT_{\rm ex})-1\}^2}$.

Error Estimates for Optical-Depth-Corrected Brightness Temperature

As described in §4, the optical-depth-corrected main beam brightness temperature, $T_{\rm mb}^{\rm corr}$, is given by

$$T_{\rm mb}^{\rm corr} = \frac{\tau T_{\rm mb}}{1-e^{-\tau}}. \tag{A10}$$

The uncertainty, $\Delta T_{\rm mb}^{\rm corr}$, at each velocity channel is calculated through

$$\Delta T_{\rm mb}^{\rm corr} = \left(\frac{\partial T_{\rm mb}^{\rm corr}}{\partial T_{13}}\right) \Delta T_{13}^{\rm rms} + \left(\frac{\partial T_{\rm mb}^{\rm corr}}{\partial \tau}\right) \Delta\tau_{\rm rms} \tag{A11}$$

where $\frac{\partial T_{\rm mb}^{\rm corr}}{\partial\tau} = \frac{1}{1-e^{-\tau}} + \frac{\tau e^{-\tau}}{(1-e^{-\tau})^2}$ and $\frac{\partial T_{\rm mb}^{\rm corr}}{\partial T_{13}} = \frac{\tau}{1-e^{-\tau}}$. Notice that the optical depth error in Eq.(A11), $\Delta\tau_{\rm rms}$, is given by Eq.(A8) for Cases (i) and (ii), and is given through the error analysis described in Appendix A.3.2 for Case (iii). One can see that the mean $\Delta T_{\rm mb}^{\rm corr}$ values, which are obtained by averaging $\Delta T_{\rm mb}^{\rm corr}(v)$ values along the velocity axis at each map position, are enhanced towards the GF 9-2 dense cloud core. This is most likely because $\Delta\tau_{\rm rms}$ values showed relatively large ones towards the core (see Figure 20). The mean $\langle \Delta T_{\rm mb}^{\rm corr}\rangle$ all over the observed area was 1.5 K (median = 1.4) with standard deviation of 0.66 K.

ERROR ESTIMATES FOR SPECTRAL MOMENTA

In the following subsections, we present our error estimate for the spectral moment calculations described in §4.3. The resultant error maps are shown in Figure 22.

Error Estimates for the Zeroth Moment

The zeroth spectral moment along the velocity axis, corresponding to the integrated intensity in unit of K·km s^{-1}, is defined by $I = \int T(v)dv$, and is calculated by

$$I = \sum_{i=1}^{N} T_{{\rm mb},i}^{\rm corr} \Delta v \tag{B1}$$

over N velocity channels where the emission exceeds the detection threshold. Here $T_{\rm mb}^{\rm corr}$ is given by Eq.(A10), and Δv denotes the width of each velocity channel. Given the definition, the error of the zeroth moment is written by

$$\Delta I = \sqrt{\sum_{i=1}^{N} \left(\frac{\partial I}{\partial T_{{\rm mb},i}^{\rm corr}}\right)^2 \left(\Delta T_{{\rm mb},i}^{\rm corr}\right)^2}, \tag{B2}$$

and is calculated as,

$$\Delta I = \sqrt{(\Delta v)^2 \sum_{i=1}^{N} \left(\Delta T_{{\rm mb},i}^{\rm corr}\right)^2}. \tag{B3}$$

Figure 22a presents the error map of the zeroth moment, which is similar to the total integrated intensity map (Figure 2). The mean ΔI calculated over whole the region is 3.5 K·km s^{-1} (median = 3.5 K·km s^{-1}) with standard deviation of 0.88 K·km s^{-1}. Comparing Figure 10a with Figure 22a, the uncertainties are about 60% with respect to the total intensities.

Error Estimates for the First Moment

The first moment, which gives an intensity-weighted mean velocity, i.e., centroid velocity ($v_{\rm cent}$), is defined by $v_{\rm cent} = \frac{\int T(v) v dv}{\int T(v) dv}$. This should be calculated by,

$$v_{\rm cent} = \frac{\sum_{i=1}^{N} v_i T_{{\rm mb},i}^{\rm corr}}{\sum_{i=1}^{N} T_{{\rm mb},i}^{\rm corr}}. \tag{B4}$$

Therefore the uncertainty of $v_{\rm cent}$ is given by,

$$\Delta v_{\rm cent} = \sqrt{\sum_{i=1}^{N} \left(\frac{\partial v_{\rm cent}}{\partial v_i}\right)^2 (\Delta v_i)^2 + \sum_{i=1}^{N} \left(\frac{\partial v_{\rm cent}}{\partial T_{{\rm mb},i}^{\rm corr}}\right)^2 \left(\Delta T_{{\rm mb},i}^{\rm corr}\right)^2}. \tag{B5}$$

Here Δv_i is the uncertainty in the LSR-velocity at the i-th channel, which can be replaced by the velocity resolution of the spectrometer, $\Delta v_{\rm res}$. Since $\Delta v_{\rm res}$ is generally represented by FWHM of the window function of the spectrometer ($\Delta v_{\rm FWHM}$), one has to divide it by $\sqrt{8\ln 2}$ to obtain the uncertainty in velocity, i.e., standard deviation. We thus obtained the equation below for computing error associated with the centroid velocity as,

$$\Delta v_{\rm cent} = \sqrt{\sum_{i=1}^{N} \left(\frac{T_{{\rm mb},i}^{\rm corr}}{I}\right)^2 \left(\frac{\Delta v_{\rm FWHM}}{\sqrt{8\ln 2}}\right)^2 + \sum_{i=1}^{N} \left(\frac{v_i - v_{\rm cent}}{I}\right)^2 \left(\Delta T_{{\rm mb},i}^{\rm corr}\right)^2}. \tag{B6}$$

Figure 22b shows the error map of $\Delta v_{\rm cent}$; the mean value $\langle \Delta v_{\rm cent} \rangle$ over the observed region is 0.27 km s^{-1} (median = 0.26 km s^{-1}) with standard deviation of 0.07 km s^{-1}. The $\Delta v_{\rm cent}$ map seems fairly "flat" compared with that of the ΔI. This is probably because estimating velocity width is principally sensitive to the dual terminal LSR-velocities at each spectrum, whereas ΔI is generally sensitive to the peak value of the spectrum.

Error Estimates for the Second Moment

The second moment, which corresponds to the intensity-weighted velocity dispersion, is defined by $\sigma = \sqrt{\frac{\int T(v)(v-v_{\rm cent})^2 dv}{\int T(v) dv}}$. In practice, we adopt a definition of

$$\sigma = \sqrt{\frac{\sum_{i=1}^{N} (v_i - v_{\rm cent})^2 T_{{\rm mb},i}^{\rm corr}}{\sum_{i=1}^{N} T_{{\rm mb},i}^{\rm corr}}}. \tag{B7}$$

This leads to the uncertainty of the velocity dispersion as

$$\Delta\sigma = \sqrt{\sum_{i=1}^{N} \left(\frac{\partial \sigma}{\partial v_i}\right)^2 \left(\frac{\Delta v_{\rm FWHM}}{\sqrt{8\ln 2}}\right)^2 + \sum_{i=1}^{N} \left(\frac{\partial \sigma}{\partial T_{{\rm mb},i}^{\rm corr}}\right)^2 \left(\Delta T_{{\rm mb},i}^{\rm corr}\right)^2}, \tag{B8}$$

where $\frac{\partial \sigma}{\partial v_i} = \frac{1}{\sigma I^2}\left\{(v_i - v_{\rm cent}) T_{{\rm mb},i}^{\rm corr} I - \sum_{i=j}^{N} (v_j - v_{\rm cent}) \left(T_{{\rm mb},i}^{\rm corr}\right)^2\right\}$ and $\frac{\partial \sigma}{\partial T_{{\rm mb},i}^{\rm corr}} = \frac{1}{2\sigma I}\left\{(v_i - v_{\rm cent})^2 - 3\sigma^2\right\}$. Figure 22c shows the $\Delta\sigma$ map whose mean over the observed area, $\langle \Delta\sigma \rangle$, is

0.44 km s^{-1} (median = 0.42 km s^{-1}) with standard deviation of 0.13 km s^{-1}. The $\Delta\sigma$ map appears to be insensitive to the uncertainty in determination of the terminal LSR-velocities. This is probably because velocity dispersions are calculated over the velocity ranges having the 50% level intensity with respect to the peak.

CALCULATION OF THE ^{13}CO COLUMN DENSITY AND ERROR ESTIMATE

The column density of ^{13}CO molecules ($N_{^{13}\mathrm{CO}}$) can be calculated from the total integrated intensity, i.e., the zeroth spectral moment, of the transition from the $J+1$ to J state, where J is the rotational quantum number, by assuming LTE:

$$N_{^{13}\mathrm{CO}} = \frac{3k}{8\pi^3\mu^2 B}\,\frac{(\langle T_{\rm ex}\rangle + hB/3k)}{J+1}\,\frac{\exp[hBJ(J+1)/k\langle T_{\rm ex}\rangle]}{1-\exp(-h\nu/k\langle T_{\rm ex}\rangle)}\,\frac{\int T_{\rm mb}^{\rm corr}(v)dv}{J_\nu(\langle T_{\rm ex}\rangle)-J_\nu(T_{\rm bg})}, \tag{C1}$$

where μ is the dipole moment of ^{13}CO (0.1101 debye), B the rotational constant (55101.0138 MHz) (See e.g., Appendix B of paper I and references therein), and $\langle T_{\rm ex}\rangle$ is the mean excitation temperature averaged along the LSR-velocity axis at each pixel position (Figure 8).

Since Eq.(C1) is a function of $\langle T_{\rm ex}\rangle$ and $I\left(=\int T_{\rm mb}^{\rm corr}(v)dv\right)$, its uncertainty is given by,

$$\Delta N_{^{13}\mathrm{CO}} = \sqrt{\left(\frac{\partial N_{^{13}\mathrm{CO}}}{\partial\langle T_{\rm ex}\rangle}\right)^2(\Delta\langle T_{\rm ex}\rangle)^2 + \left(\frac{\partial N_{^{13}\mathrm{CO}}}{\partial I}\right)^2(\Delta I)^2}. \tag{C2}$$

In Appendix A.2 and B.1, we showed that $T_{\rm ex}$ has typical uncertainty of 15%, while I has much larger uncertainty of 60%. Therefore, ignoring the first term, Eq.(C2) can be approximated by

$$\Delta N_{^{13}\mathrm{CO}} \simeq \frac{\partial N_{^{13}\mathrm{CO}}}{\partial I}\Delta I. \tag{C3}$$

Another method of estimating $\Delta N_{^{13}\mathrm{CO}}$ is as follows. Since Eq.(C2) becomes a rather complicated formula given by a function of $\langle T_{\rm ex}\rangle$ and I, we numerically estimated $\Delta N_{^{13}\mathrm{CO}}$ by changing $\langle T_{\rm ex}\rangle$ values by $\pm\Delta\langle T_{\rm ex}\rangle$ and I values by $\pm\Delta I$. Namely, we assumed that the real $\Delta N_{\rm tot}$ value would be smaller than an upper limit of $N_{\rm tot}^{\rm upper}$ which may be obtained when $\langle T_{\rm ex}\rangle = \langle T_{\rm ex}\rangle + \Delta\langle T_{\rm ex}\rangle$ and $I = I + \Delta I$. The $N_{^{13}\mathrm{CO}}^{\rm lower}$ is calculated with the similar fashion. We thus adopted

$$\Delta N_{^{13}\mathrm{CO}} \simeq \frac{1}{2}(N_{^{13}\mathrm{CO}}^{\rm upper} - N_{^{13}\mathrm{CO}}^{\rm lower}). \tag{C4}$$

The resultant $\Delta N_{^{13}\mathrm{CO}}$ maps produced from the two methods expressed by Eqs.(C3) and (C4) agree with each other within uncertainty of $\sim$2%. We therefore arbitrary adopted the map calculated by Eq.(C4) (Figure 23), which is further used in the analysis discussed in §5.5. Figure 23 presents a summary of our uncertainty estimate. The resultant $\Delta N_{\rm H_2}/N_{\rm H_2}$ map has a mean uncertainty of 68% with a standard deviation of 12%.

DATA SELECTION CRITERIA FOR PRODUCING THE MAPS OF MEAN EXCITATION TEMPERATURE, SPECTRAL MOMENTA, AND COLUMN DENSITY

As summarized in the end of Appendix A.2, we obtained the solutions at a total of 36622 positions in the 3D space of ($\Delta\alpha$, $\Delta\delta$, $V_{\rm LSR}$). Using the results from error calculations in Appendices A.3 and A.4, we checked whether or not the 36622 solutions satisfy the following three conditions:

$$\begin{aligned} \tau &> \Delta\tau, \\ T_{\rm ex} &> \Delta T_{\rm ex}, \\ \text{and} \\ T_{\rm mb}^{\rm corr} &> \Delta T_{\rm mb}^{\rm corr}. \end{aligned} \tag{D1}$$

A total of 35916 points in the 3D space (98.1%) passed the above test; 34664 points from Case (i), 783 points from Case (ii), and 449 points from Case (iii), corresponding to 2923, 304, and 328 positions in the ($\Delta\alpha$, $\Delta\delta$) space. Furthermore, we discarded 21 points which do not satisfy a set of empirical conditions of

$$\begin{aligned} 0.1 < \tau &< 10.0, \\ \Delta\tau &< 0.01, \\ \text{and} \\ 14.5 > T_{\rm ex}/\mathrm{K} &> T_{\rm bg} - \langle\Delta T_{\rm ex}^{\rm rms}\rangle. \end{aligned} \tag{D2}$$

The limit values of 0.1 and 0.01 in the first and second conditions, respectively, were given by the accuracy in our calculations. The numerical upper limits in the first and third conditions are fiducial values obtained from "trials-and-errors". Eventually, we obtained reliable solutions at a total of 35895 positions in the ($\Delta\alpha$, $\Delta\delta$, $V_{\rm LSR}$) space (see

Figures 7, 8, 20, and 21), yielding 3555 spatial positions in the ($\Delta\alpha$, $\Delta\delta$) space. Namely, we eventually obtained a total of 3555 optical-depth-corrected ^{13}CO spectra in the 72×72 =5184 observed positions. Here we accepted the 20 points obtained from Case (iv) which are required to pass only the first and third conditions in Eq.(D2). This is because we were unable to estimate the uncertainties of $\Delta\tau$, $\Delta T_{\rm ex}$, and $\Delta T_{\rm mb}^{\rm corr}$ in Case (iv) (see Appendix A.2). Towards the central regions of the $V_{\rm LSR}$= -2.1 and -1.9 km s^{-1} panels in Figures 7 and 8, we could not obtain reliable τ and $T_{\rm ex}$ solutions owing to the three conditions in Eq. (D2).

Subsequently we performed momentum analysis to the 3555 spectra, as described in Appendix B. For this purpose, one needs to define an LSR-velocity range over which the spectrum moments are calculated. We defined the range by two terminal velocities of $v_{\rm t,blue}$ and $v_{\rm t,red}$ where the $T_{\rm mb}^{\rm corr}(v)$ spectra first drop below the 3σ levels in searching from the peak LSR-velocity toward the blue- and redward directions, respectively. After several iterations, we found that the conditions of,

$$\begin{aligned} v_{\rm t,blue} < v_{\rm cent} < v_{\rm t,red}, \\ |v_{\rm t,blue} - v_{\rm t,red}| > \sigma > \Delta\sigma > \tfrac{\Delta v_{\rm res}}{\sqrt{8\ln 2}}, \\ I > \Delta I, \\ \langle T_{\rm ex}\rangle > T_{\rm bg}, \end{aligned} \tag{D3}$$

and

$$N_{^{13}\rm CO} > \Delta N_{^{13}\rm CO}$$

give the most reasonable results for Figures 9, 10, 11, 22 and 23. In these figures, a total of 3093 spatial positions out of 3555 are presented. Here $\frac{\Delta v_{\rm res}}{\sqrt{8\ln 2}}$ is calculated to be 0.0425 km s^{-1} (see §2).

ERROR ESTIMATE OF THE FILAMENT SCALE HEIGHT

In our model analysis based on the Stodolkiewicz-Ostriker cylinder (§5.3.1), the averaged radial column density profile shown in Figure 15 was analyzed considering the uncertainty of each column density, $\Delta N_{\rm H_2}$, obtained from Figure 23 (see also Appendix C). Then the uncertainty in the best-fit scale height H of $\Delta H = 0.02$ was determined from the interval between the minimum χ^2 value $\chi^2_{\rm min}$ (20.8) and $\chi^2_{\rm min}+1$, as shown in Figure 24. Since the degree of freedom is 27, the reduced $\chi^2_{\rm min}$ value becomes 0.77.

In addition, we can analytically derive the uncertainty of H from the following approximate equation of,

$$\Delta H \sim \frac{\Delta\chi^2}{\frac{\partial\chi^2}{\partial H}} \sim \frac{1}{\frac{N}{H}} = \frac{H}{N} \quad \text{for } r < H, \tag{E1}$$

yielding $\Delta H = 0.02$ for the number of the data points of $N = 28$.

REFERENCES

Allen, A., & Shu, F. H. 2000, ApJ, 536, 368
André, P., Basu, S., & Inutsuka, S. 2009, Structure Formation in Astrophysics, 254
André, P., Men'shchikov, A., Bontemps, S., et al. 2010, A&A, 518, L102
Arzoumanian, D., André, P., Didelon, P., et al. 2011, A&A, 529, L6
Barranco, J. A., & Goodman, A. A. 1998, ApJ, 504, 207
Bodenheimer, P. H. 2011, Principles of Star Formation: , Astronomy and Astrophysics Library. ISBN 978-3-642-15062-3. Springer-Verlag Berlin Heidelberg, 2011,
Bontemps, S., Andre, P., Terebey, S., & Cabrit, S. 1996, A&A, 311, 858
Caselli, P., Benson, P. J., Myers, P. C., & Tafalla, M. 2002, ApJ, 572, 238
Ciardi, D. R., Woodward, C. E., Clemens, D. P., Harker, D. E., & Rudy, R. J. 1998, AJ, 116, 349
Ciardi, D. R., Woodward, C. E., Clemens, D. P., Harker, D. E., & Rudy, R. J. 2000, AJ, 120, 393
Chandrasekhar, S., & Fermi, E. 1953a, ApJ, 118, 113
Chandrasekhar, S., & Fermi, E. 1953b, ApJ, 118, 116
Chapman, N. L., Goldsmith, P. F., Pineda, J. L., et al. 2011, ApJ, 741, 21
Crutcher, R. M. 2004, Ap&SS, 292, 225
Dickman, R. L. 1978, ApJS, 37, 407
Elmegreen, B. G. 2007, ApJ, 668, 1064
Furuya, R. S., Kitamura, Y., & Shinnaga, H. 2006, ApJ, 653, 1369 (paper I)
Furuya, R. S., Kitamura, Y., & Shinnaga, H. 2008, PASJ, 60, 421(paper II)
Furuya, R. S., Kitamura, Y., & Shinnaga, H. 2009, ApJ, 692, 96 (paper III)
Furuya, R. S., Kitamura, Y., & Shinnaga, H. 2014, D. Stamatellos et al. (eds.), *The Labyrinth of Star Formation*, Astrophysics and Space and Science Proceedings 36, Springer International Publishing Switzerland, in press
Frerking, M. A., Langer, W. D., & Wilson, R. W. 1982, ApJ, 262, 590
Garden, R. P., Hayashi, M., Hasegawa, T., Gatley, I., & Kaifu, N. 1991, ApJ, 374, 540
Goldsmith, P. F., Heyer, M., Narayanan, G., et al. 2008, ApJ, 680, 428
Goodman, A. A., Barranco, J. A., Wilner, D. J., & Heyer, M. H. 1998, ApJ, 504, 223
Hartmann, L., Ballesteros-Paredes, J., & Bergin, E. A. 2001, ApJ, 562, 852
Hacar, A., & Tafalla, M. 2011, A&A, 533, A34

Hacar, A., Tafalla, M., Kauffmann, J., & Kovács, A. 2013, A&A, 554, A55
Hanawa, T., Nakamura, F., Matsumoto, T., et al. 1993, ApJ, 404, L83
Heitsch, F., Ballesteros-Paredes, J., & Hartmann, L. 2009, ApJ, 704, 1735
Heyer, M., Gong, H., Ostriker, E., & Brunt, C. 2008, ApJ, 680, 420
Hunter, C. 1977, ApJ, 218, 834
Inutsuka, S.-I., & Miyama, S. M. 1992, ApJ, 388, 392
Inutsuka, S.-i., & Miyama, S. M. 1997, ApJ, 480, 681
Kainulainen, J., Beuther, H., Henning, T., & Plume, R. 2009, A&A, 508, L35
Klessen, R. S., Heitsch, F., & Mac Low, M.-M. 2000, ApJ, 535, 887
Klessen, R. S., Ballesteros-Paredes, J., Vázquez-Semadeni, E., & Durán-Rojas, C. 2005, ApJ, 620, 786
Krumholz, M. R., & McKee, C. F. 2005, ApJ, 630, 250
Krumholz, M. R., & Tan, J. C. 2007, ApJ, 654, 304
Lang, K. R. 1980, Astrophysical Formulae. A Compendium for the Physicist and Astrophysicist., ed. K. R. Lang (Berlin: Springer), 563
Larson, R. B. 1969, MNRAS, 145, 271
Larson, R. B. 1985, MNRAS, 214, 379
Leão, M. R. M., de Gouveia Dal Pino, E. M., Santos-Lima, R., & Lazarian, A. 2013, ApJ, 777, 46
Lequeux, J. 2005, The Interstellar Medium (Berlin: Springer)
Mac Low, M.-M. 1999, ApJ, 524, 169
Mac Low, M.-M., & Klessen, R. S. 2004, Reviews of Modern Physics, 76, 125
Men'shchikov, A., André, P., Didelon, P., et al. 2010, A&A, 518, L103
Miyama, S. M., Hayashi, C., & Narita, S. 1984, ApJ, 279, 621
Nagasawa, M. 1987, Progress of Theoretical Physics, 77, 635
Nakamura, F., & Li, Z.-Y. 2005, ApJ, 631, 411
Nakamura, F., & Li, Z.-Y. 2007, ApJ, 662, 395
Nakamura, F., & Li, Z.-Y. 2008, ApJ, 687, 354
Nutter, D., Kirk, J. M., Stamatellos, D., & Ward-Thompson, D. 2008, MNRAS, 384, 755
Ossenkopf, V., & Mac Low, M.-M. 2002, A&A, 390, 307
Ostriker, J. 1964, ApJ, 140, 1056
Ostriker, E. C., Stone, J. M., & Gammie, C. F. 2001, ApJ, 546, 980
Padoan, P., & Nordlund, Å. 1999, ApJ, 526, 279
Padoan, P., Juvela, M., Goodman, A. A., & Nordlund, Å. 2001, ApJ, 553, 227
Padoan, P., & Nordlund, Å. 2002, ApJ, 576, 870
Palmeirim, P., André, P., Kirk, J., et al. 2013, A&A, 550, A38
Palla, F., & Stahler, S. W. 2002, ApJ, 581, 1194
Penston, M. V. 1969, MNRAS, 144, 425
Phillips, T. G., Huggins, P. J., Wannier, P. G., & Scoville, N. Z. 1979, ApJ, 231, 720
Pineda, J. E., Goodman, A. A., Arce, H. G., et al. 2010, ApJ, 712, L116
Poidevin, F., & Bastien, P. 2006, ApJ, 650, 945
Plummer, H. C. 1911, MNRAS, 71, 460
Sawada, T., et al. 2008, PASJ, 60, 445
Schneider, S., & Elmegreen, B. G. 1979, ApJS, 41, 87
Shu, F. H. 1977, ApJ, 214, 488
Shu, F. H. 1992, The physics of astrophysics. Volume II: Gas dynamics., by Shu, F. H.. University Science Books, Mill Valley, CA (USA), 1992,
Spitzer, L., Jr. 1978, Physical Processes in the Interstellar Medium (New York: Academic)
Stahler, S. W., & Palla, F. 2005, The Formation of Stars, by Steven W. Stahler, Francesco Palla, pp. 865. ISBN 3-527-40559-3. Wiley-VCH , January 2005
Stodólkiewicz, J. S. 1963, Acta Astron., 13, 30
Vázquez-Semadeni, E., Passot, T., & Pouquet, A. 1996, ApJ, 473, 881
Vázquez-Semadeni, E., Kim, J., Shadmehri, M., & Ballesteros-Paredes, J. 2005, ApJ, 618, 344
White, R. E. 1977, ApJ, 211, 744

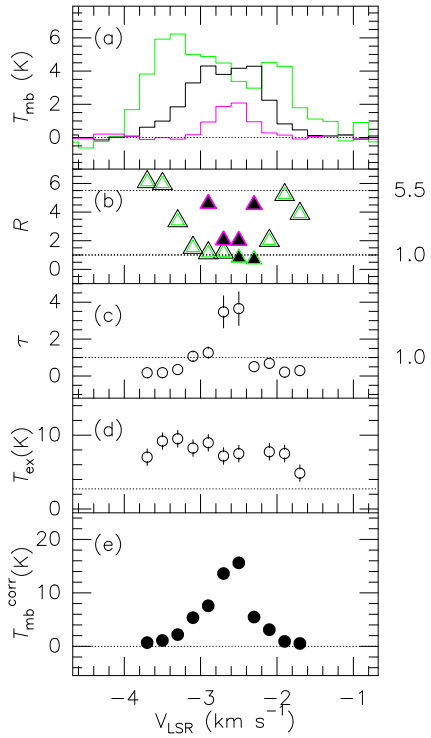

Figure 18. corresponding to Appendix Fig.1. Example of our analysis to estimate the ^{13}CO optical depth (τ; panel c) and excitation temperature ($T_{\rm ex}$; panel d) for obtaining an opacity-corrected $T_{\rm mb}$ spectrum of the ^{13}CO line (panel e). The panel (a) shows the ^{12}CO (green), ^{13}CO (black), and C^{18}O (magenta) spectra in the $T_{\rm mb}$ scale towards the position of the 3 mm continuum source (paper I). The panel (b) represents intensity ratios between the ^{12}CO and ^{13}CO lines [$R_{12/13} = T_{\rm mb}(^{12}{\rm CO})/T_{\rm mb}(^{13}{\rm CO})$; black-and-green triangles] and between the ^{13}CO and C^{18}O lines [$R_{13/18} = T_{\rm mb}(^{13}{\rm CO})/T_{\rm mb}(^{18}{\rm CO})$; magenta-and-black triangles]. See Appendix *A*.2 for details.

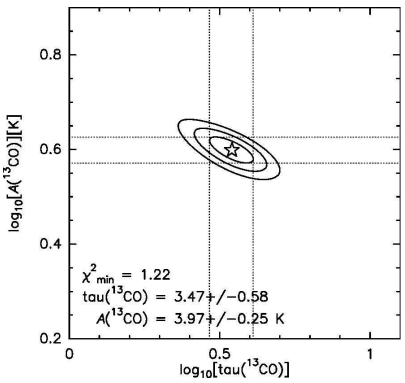

Figure 19. corresponding to Appendix Fig.2. Contour map showing the "confidence region boundaries" for the case (iii) in our analysis as a function of the optical depth and the quantity A, defined in Appendix A.2, of the ^{13}CO emission. This plot represents an example for a velocity channel of $V_{\rm LSR}$= −2.6 km s^{-1} for the spectra shown in Figure 18. The central star indicates the position where the minimum χ^2, $\chi^2_{\rm min}$, of 1.22 is found. The three contours show the levels of $\chi^2_{\rm min} + 2.30$, $\chi^2_{\rm min} + 6.18$, and $\chi^2_{\rm min} + 11.8$, corresponding to the confidence levels of 68.3%, 95.45%, and 99.73%, respectively. The interval between the two dashed lines on each axis gives the 1σ error for the corresponding parameter.

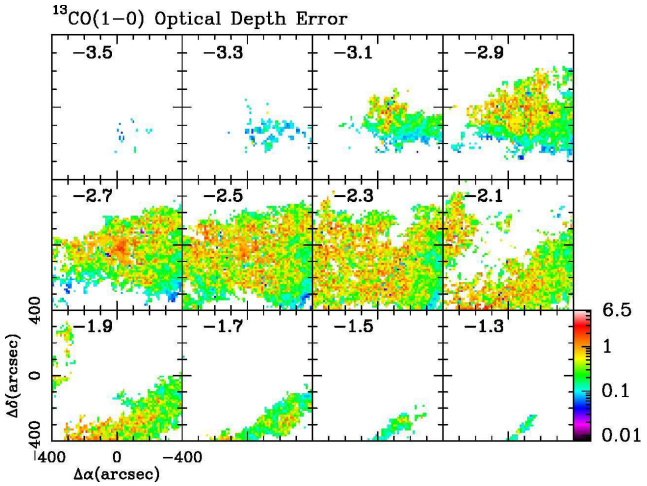

Figure 20. corresponding to Appendix Fig.3. Velocity channel maps of the errors of the ^{13}CO optical depth maps shown in Figure 7. The central LSR-velocity of each velocity channel in km s^{-1} is shown in each panel. See Appendix A.3 for details.

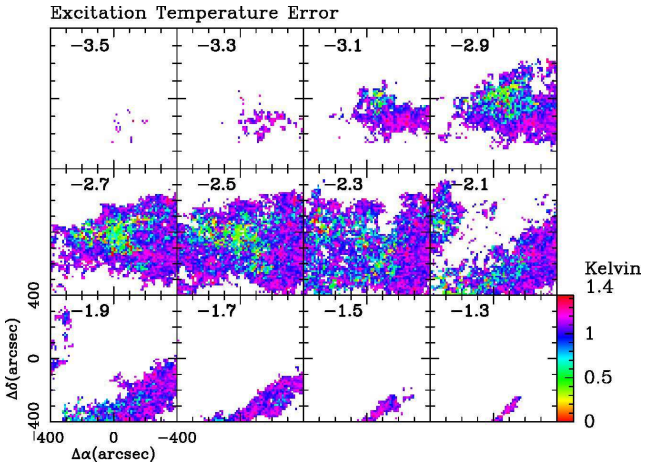

Figure 21. corresponding to Appendix Fig.4. Velocity channel maps of the errors of the ^{13}CO excitation temperature maps shown in Figure 8. Notice that the error is shown in linear scale. See Appendix A.3 for details.

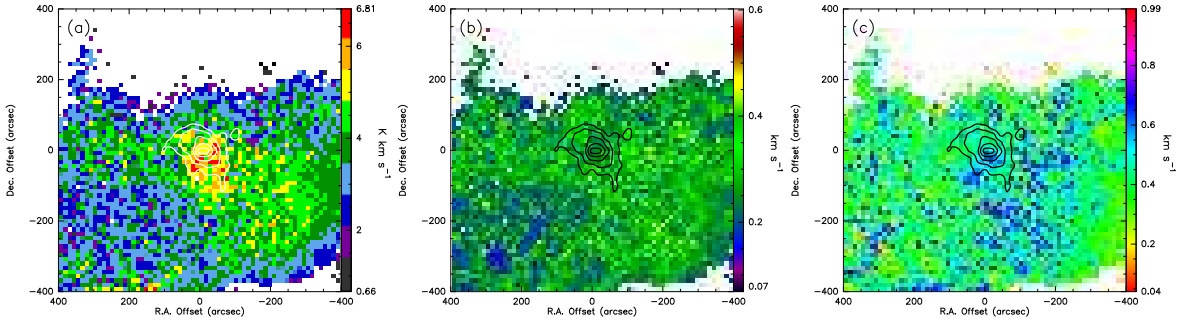

Figure 22. corresponding to Appendix Fig.5. Uncertainty maps of (a) the total intensity in K km s^{-1}, (b) centroid velocity in km s^{-1}, and (c) velocity dispersion in km s^{-1} for the Component 1. These maps are produced in the spectral moment analysis for the opacity-corrected ^{13}CO (1–0) spectra, as described in Appendix B, and are shown in the same manner as in Figure 10.

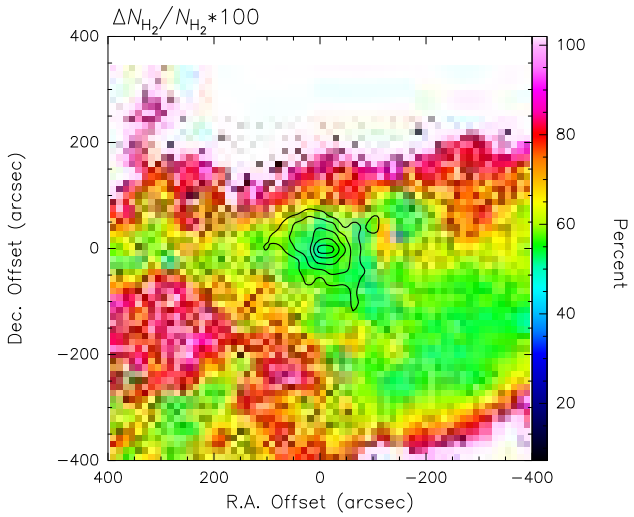

Figure 23. corresponding to Appendix Fig.6. Map of the uncertainty of molecular hydrogen column density defined by $\Delta N_{\rm H_2}/N_{\rm H_2}$. See Appendix C for details.

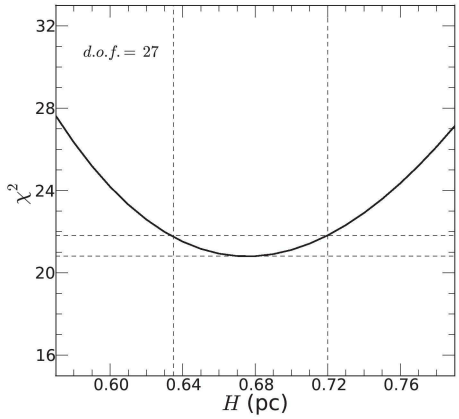

Figure 24. corresponding to Appendix Fig.7. Plot of the scale height H vs. χ^2-values in the radial column density profile analysis shown in Figure 15 (see also §5.3.1); the degree of freedom ($d.o.f.$) is 27. The lower and upper horizontal dashed lines present the minimum χ^2-value of $\chi^2_{\rm min}$ and the $\chi^2_{\rm min} + 1.0$ value, respectively. The interval between the two vertical dashed lines gives the 1σ uncertainty in H of $\Delta H = 0.04\,$pc. See Appendix E.